Screened hybrid functional applied to $3d^0 \rightarrow 3d^8$ transition-metal perovskites LaMO_3 (M = Sc–Cu): Influence of the exchange mixing parameter on the structural, electronic, and magnetic properties

Jiangang He and Cesare Franchini
University of Vienna, Faculty of Physics and Center for Computational Materials Science, Vienna, Austria
(Received 16 September 2012; published 13 December 2012)

We assess the performance of the Heyd-Scuseria-Ernzerhof (HSE) screened hybrid density functional scheme applied to the perovskite family LaMO_3 (M = Sc–Cu) and discuss the role of the mixing parameter α [which determines the fraction of exact Hartree-Fock exchange included in the density functional theory (DFT) exchange-correlation functional] on the structural, electronic, and magnetic properties. The physical complexity of this class of compounds, manifested by the largely varying electronic characters (band/Mott-Hubbard/charge-transfer insulators and metals), magnetic orderings, structural distortions (cooperative Jahn-Teller–type instabilities), as well as by the strong competition between localization/delocalization effects associated with the gradual filling of the t_{2g} and e_g orbitals, symbolize a critical and challenging case for theory. Our results indicate that HSE is able to provide a consistent picture of the complex physical scenario encountered across the LaMO_3 series and significantly improve the standard DFT description. The only exceptions are the correlated paramagnetic metals $LaNiO_3$ and $LaCuO_3$, which are found to be treated better within DFT. By fitting the ground-state properties with respect to α, we have constructed a set of "optimum" values of α from $LaScO_3$ to $LaCuO_3$: it is found that the optimum mixing parameter decreases with increasing filling of the d manifold ($LaScO_3$: 0.25; $LaTiO_3$ and $LaVO_3$: 0.10–0.15; $LaCrO_3$, $LaMnO_3$, and $LaFeO_3$: 0.15; $LaCoO_3$: 0.05; $LaNiO_3$ and $LaCuO_3$: 0). This trend can be nicely correlated with the modulation of the screening and dielectric properties across the LaMO_3 series, thus providing a physical justification to the empirical fitting procedure. Finally, we show that by using this set of optimum mixing parameter, HSE predict dielectric constants in very good agreement with the experimental ones.

DOI: 10.1103/PhysRevB.86.235117 PACS number(s): 71.27.+a, 71.15.−m, 71.10.−w, 71.28.+d

I. INTRODUCTION

The physics of transition-metal perovskites with general chemical formula ABO_3 [where A is a large cation, similar in size to O^{2-} and B is a small transition-metal (TM) cation] has attracted and challenged the interest and curiosity of the material science community for many decades due to huge variety of complex phenomena arising from the subtle coupling between structural, electronic, and magnetic degrees of freedom. The high degree of chemical flexibility and the localized (i.e., not spatially homogeneous) character of the dominant TM partially filled d states lead to the coexistence of several physical interactions (spin, charge, lattice, and orbital), which are all simultaneously active. The occurrence of strong lattice-electron, electron-spin, and spin-orbit couplings causes several fascinating phenomena, including metal-insulator transitions,[1,2] superconductivity,[3] colossal magnetoresistance,[4,5] multiferroicity,[6] band gaps spanning the visible and ultraviolet,[7] and surface chemical reactivity from active to inert.[8,9] When the additional degrees of freedom afforded by the combinatorial assemblage of perovskite building blocks in superlattices, heterointerfaces, and thin films are introduced, the range of properties increases all the more, as demonstrated by the recent several remarkable discoveries in the field of oxide heterostructures.[10] Tunability and control of these intermingled effects can be further achieved by means of external stimuli such as doping,[11,12] pressure,[13,14] temperature, and magnetic or electric fields,[15,16] thereby enhancing the tailoring capability of perovskites for a wide range of functionalities. This rich array of behaviors uniquely suit perovskites for novel solutions in different sectors of modern technology [optoelectronics, spintronics, piezoelectric devices, and (photo)catalysis], for which conventional semiconductors can not be used.[17–20]

Theoretical studies of TM perovskites, aiming to describe and understand the underlying physical mechanisms determining their complex electronic structures, have been mainly developed within two historically distinct solid-state communities, i.e., model Hamiltonians[21,22] and *first principles,*[23] which in recent years have initiated to fruitfully cross connect each other's methodologies towards more general schemes such as DFT + DMFT (density functional theory[24] + dynamical mean-field theory[25–27]), with the aim to overtake the individual limitations and to improve the applicability and predictive power of electronic-structure theory.[28,29] Model Hamiltonian approaches adopt simplified lattice fermion models, typically the celebrated *Hubbard model*, inspired by the seminal works of Anderson,[30] Hubbard,[31] and Kanamori[32] in which the many-body problem is solved using a small number of *relevant* bands and short-ranged electron interactions. These effective models can solve the many-body problem very accurately, also including ordering and quantum fluctuations, but critically depend on a large number of adjustable parameters (which can be in principle derivable by *first-principles* schemes[33,35,38–41]), and its applicability is restricted to finite-size systems.[2,29] In DFT, the intractable many-body problem of interacting electrons is mapped into a simplified problem of noninteracting electrons moving in an effective potential throughout the Kohn-Sahm scheme,[24] and electron exchange-correlation (XC) effects are accounted by the XC potential which is approximated using XC functionals such as the local density approximation (LDA), the generalized gradient approximation

TABLE I. Summary of the fundamental ground-state properties of LaMO$_3$: (i) crystal structure: O = orthorhombic, M = monoclinic, R = rhombohedral, and T = tetragonal; (ii) transition-metal (TM) spin-projected electronic configuration and (line below) corresponding oxidation state, (iii) electronic character: I = insulator and M = metal; magnetic ordering: NM nonmagnetic, different type of AFM arrangements (see Fig. 1), and PM = paramagnetic.

	LaScO$_3$	LaTiO$_3$	LaVO$_3$	LaCrO$_3$	LaMnO$_3$	LaFeO$_3$	LaCoO$_3$	LaNiO$_3$	LaCuO$_3$
Crystal structure	O-P_{nma}	O-P_{nma}	M-$P_{2_1/b}$	O-P_{nma}	O-P_{nma}	O-P_{nma}	R-$R_{\bar{3}c}$	R-$R_{\bar{3}c}$	T-$P_{4/m}$
TM electronic configuration	d^0	$t_{2g}{}^{\uparrow}$	$t_{2g}{}^{\uparrow\uparrow}$	$t_{2g}{}^{\uparrow\uparrow\uparrow}$	$t_{2g}{}^{\uparrow\uparrow\uparrow}e_g{}^{\uparrow}$	$t_{2g}{}^{\uparrow\uparrow\uparrow}e_g{}^{\uparrow\uparrow}$	$t_{2g}{}^{\uparrow\downarrow\uparrow\downarrow\uparrow\downarrow}$	$t_{2g}{}^{\uparrow\downarrow\uparrow\downarrow\uparrow\downarrow}e_g{}^{\uparrow}$	$t_{2g}{}^{\uparrow\downarrow\uparrow\downarrow\uparrow\downarrow}e_g{}^{\uparrow\downarrow}$
	3+	3+	3+	3+	3+	3+	3+	3+	3+
Electronic character	I	I	I	I	I	I	I	M	M
Magnetic structure	NM	G-AFM	C-AFM	G-AFM	A-AFM	G-AFM	PM	PM	PM

(GGA) *et similia*.[42] As the name suggests, in DFT the ground-state properties are obtained only from the charge density, and this makes DFT fundamentally different from wave-function-based approaches as the Hartee-Fock method, the simplest approximation to the many-body problem which includes the exact exchange but no correlation.[43] Although DFT has been widely and successfully used in the last 40 years in solid-state physics and quantum chemistry to calculate structural data, energetics and, to a lesser extent, electronic and magnetic properties, it suffers of fundamental difficulties mostly due to the approximate treatment of XC effects. This drawback is particularly severe when DFT is applied to the so-called strongly correlated systems (SCSs), the prototypical examples of which are transition-metal oxides (TMOs). A systematic improvement of these XC-related deficiencies in DFT is essentially impossible, but several "beyond-DFT" approaches have been proposed which deliver much more satisfying results. The most renewed ones are the DFT + U,[44] Self Interaction Correction (SIC),[45–48] hybrid functionals,[49] and GW.[50] For a recent review on DFT and beyond applied to transition-metal oxides, see Ref. 51.

In this article, we applied the screened hybrid functional introduced by Heyd, Scuseria, and Ernzerhof[52] (HSE) to study the structural, electronic, and magnetic properties of the series of 3d TMO perovskites LaMO$_3$, with M ranging from Sc to Cu. This is a rather challenging family of compounds for electronic-structure methods for several reasons[41,53–89] (see Table I): (i) it encompasses band, Mott-Hubbard (MH), and charge-transfer (CT) insulators as well as correlated metals (the last two members of the series: LaNiO$_3$ and LaCuO$_3$);[7] (ii) different types of antiferromagnetic (AFM) orderings are encountered across the series (A-type, C-type, and G-type, graphically represented in Fig. 1), but also nonmagnetic (NM, LaScO$_3$) and paramagnetic [PM, La(Co→Cu)O$_3$] systems;[55] (iii) the dominating electronic character varies from d^0 to d^8, and ranges from t_{2g}/e_g localization (with variable crystal-field splitting between t_{2g} and e_g states) to more spatially delocalized d orbitals;[55] (iv) the crystal symmetry spans orthorhombic (O), monoclinic (M), rhombohedral (R), and tetragonal (sketches of the crystal structures is given in Fig. 2) characterized by a different level of structural distortions [Jahn-Teller (JT: staggered disproportionation of the M-O bond lengths), GdFeO$_3$-type (GFO: collective tiltings and rotations of the oxygen octahedra), monoclinic angle β].

Before describing the method and presenting the result, we briefly recall previous *ab initio* investigations of this set of compounds performed using conventional DFT and beyond-DFT methodologies. The most widely studied member of this family is certainly the classical JT-GFO distorted Mott-Hubbard AFM insulator LaMnO$_3$, but also other compounds

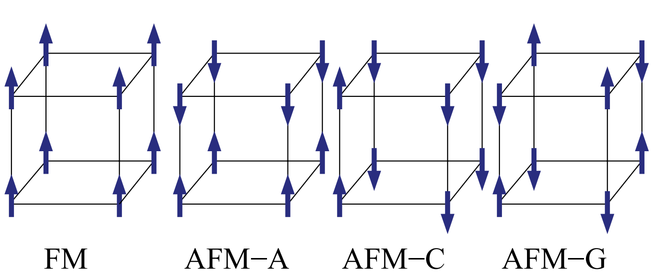

FIG. 1. (Color online) Schematic representation of the typical magnetic orderings for the perovskites.

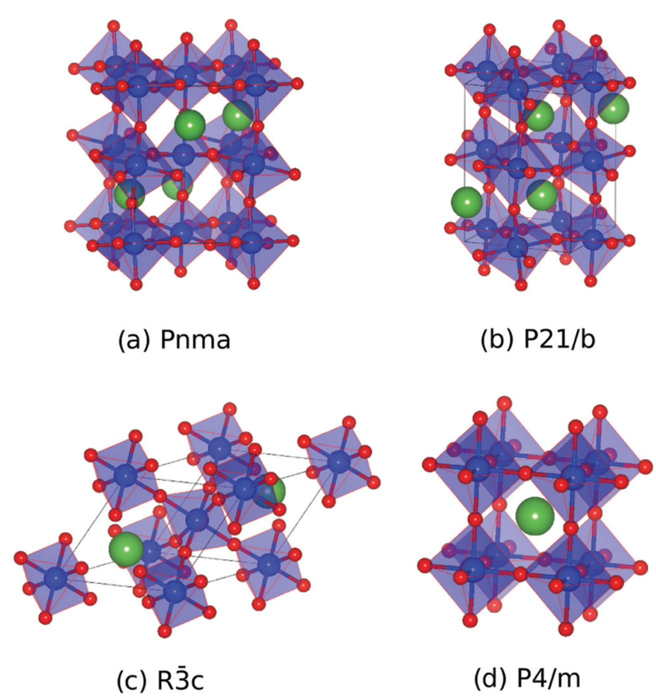

FIG. 2. (Color online) The structures of perovskite oxides studied in this paper. P_{nma} for LaScO$_3$, LaTiO$_3$, LaCrO$_3$, LaMnO$_3$, and LaFeO$_3$, $P_{2_1/b}$ for LaVO$_3$, $R_{\bar{3}c}$ for LaCoO$_3$ and LaNiO$_3$, and $P_{4/m}$ for LaCuO$_3$, respectively. The large (green), medium-sized (blue), and small (red) balls denote La, M, and O atoms, respectively. Plot done using the VESTA visualization program (Ref. 90).

have received significant attention, in particular, $LaTiO_3$ and $LaVO_3$, and to a lesser extent, $LaFeO_3$, $LaCoO_3$, $LaNiO_3$, and $LaCuO_3$. Relatively scarce studies on the band insulator $LaScO_3$ are present in literature.

DFT (Refs. 41,53,55,56,60–63,68,75,83,86,89): The seminal works of the Terakura group in the late 1990s (Refs. 55, 56,60–62) have extensively assessed the performance of LDA for the LaMO$_3$ series ($M =$ Ti–Cu), and revealed that LDA is unable to predict the observed insulating ground state for the first members ($LaTiO_3$ and $LaVO_3$), wrongly favor a nonmagnetic solution for $LaTiO_3$, and severely underestimate the insulating gap in $LaCrO_3$, $LaMnO_3$, $LaFeO_3$, and $LaCoO_3$. The situation does not improve using the GGA.[62] However, the recent GGA-based reexploration of the electronic properties of $LaCrO_3$ by Ong *et al.*[75] has reported that a good agreement with experiment can be achieved, upon a proper (re)interpretation of the optical spectra. It should be noticed that all these results were obtained using the experimental geometries. The very few structural optimizations at DFT level, mostly focused on $LaMnO_3$, have shown that although LDA/GGA reproduce the experimental volume within 1%–3%,[71,83,89] the lattice distortions associated with the JT and GFO instabilities are significantly underestimated. For compounds with more delocalized $3d$ electrons such as $LaNiO_3$, the LDA performance gets better as recently reported by Guo *et al.*[86]

DFT + U (Refs. 41,53,55,58,59,61,62,65,66,69–71,73–75, 77–81,83–86,91): In some cases, the drawbacks of LDA and GGA in treating localized partially filled d states can be adjusted by introducing a strong Hartree-Fock–type intra-atomic interaction U properly balanced by the so-called double-counting (dc) correction. The resulting LDA(GGA) + U energy functional can be written as[44]

$$E_{\rm tot}(n,\hat{n}) = E_{\rm DFT}(n) + E_{\rm HF}(\hat{n}) - E_{\rm dc}(\hat{n}), \qquad (1)$$

where $\hat{n}$ is the operator for the number of electrons occupying a particular site and n is its expectation value. This expression can be written in terms of the direct (U) and exchange (J) contributions, which lead to a set of *slightly* different LDA(GGA) + U energy functionals depending on the way the dc term is constructed.[92] Among the numerous applications of DFT + U to LaMO$_3$, the study of Solovyev and co-workers represents the most comprehensive and systematic one.[55] There it is found that LDA + U conveys a substantially improved description of the band structure of LaMO$_3$ from $LaTiO_3$ to $LaCuO_3$ with respect to conventional DFT, although the results critically depend on the specific treatment of localization effects in the $3d$ manifold. By applying the U correction to t_{2g} electrons, only the authors show that $LaTiO_3$ and $LaVO_3$ are correctly predicted to be insulating, thus curing the deficient LDA picture. At variance with DFT, $LaTiO_3$ is found to be magnetic, but with a magnetic moment twice larger than the experimental one. The band gap of early ($LaTiO_3$, $LaVO_3$) and late ($LaCoO_3$) LaMO$_3$ members which have a predominant t_{2g} character are better described than the e_g compounds $LaMnO_3$ and $LaFeO_3$, for which an onsite U applied to the entire $3d$ is needed to improve the agreement with experiment. The values of the gap clearly depend on the value of the U parameter, as discussed by Yang *et al.*[59] By fitting the U using the measured gap as reference quantity, these authors have shown that the best agreement with experiment is achieved for U progressively increasing from 5 eV ($LaCrO_3$) to 7 eV ($LaNiO_3$), about 2 eV smaller than those computed by Solovyev using constrained LDA.[55] Similarly to the standard LDA case, few attempts have been made to optimize the structural parameters at the DFT + U level[61,74,83,84,86]: (i) $LaTiO_3$: Ahn[74] and co-workers have shown that the application of LDA + U ($U = 3.2$ eV) systematically increases the (underestimated) LDA lattice parameters of $LaTiO_3$ and the internal distortions, thus improving the overall agreement with experiment. (ii) $LaMnO_3$: Using the Perdew-Burke-Ernzerhof[93] (PBE) approximation with an onsite effective $U = 2$ eV, Hashimoto *et al.*[83] have performed a full (volume and internal coordinates) structural optimization in $LaMnO_3$ and demonstrated that, unlike GGA, GGA + U accounts well for the experimental JT and tilting distortions; (iii) $LaCoO_3$: Hsu *et al.*[77] and Laref *et al.*[84] have shown that LDA + U describes well the lattice parameter, rhombohedral angle, and atomic coordinates of $LaCoO_3$; better agreement with experiment is obtained using a self-consistent U (Ref. 77) rather than a fixed U value of ≈7–8 eV.[84] (iv) $LaNiO_3$: The work of Guo *et al.*[86] on $LaNiO_3$ reported that for this correlated metal, LDA + U ($U = 6$ eV) delivers geometrical data very similar to the already satisfactory LDA ones (though, as already pointed out, LDA does a better job in predicting the electronic properties).

HF (Refs. 57,72,94): The application of a purely Hartee-Fock (HF) procedure, i.e., including an exact treatment of the exchange interaction and neglecting electron correlation, has been extensively investigated by Mizokawa and Fujimori[57] and by Solovyev.[72] Although the HF method suffers from the absence of electron correlation which is reflected by its tendency to overestimate the magnitude of band gaps (which can be cured by including the correlation effects beyond the HF approximation), these studies show that HF can qualitatively explain the ground-state electronic and magnetic properties of this class of magnetic oxides. Important exceptions are $LaNiO_3$ and $LaCuO_3$, which are found to be FM insulator ($LaNiO_3$) and G-type AFM insulator ($LaCuO_3$), in contrast with the observed PM metallic ground state. Another critical case for HF and in general for electronic-structure methods is the origin of the type-G AFM ordering in $LaTiO_3$ (Refs. 57,72,95,96): in Ref. 57 the authors report that the stabilization of the G-type arrangement can be achieved by fixing the $\mathrm{Ti} - \widehat{\mathrm{O}} - \mathrm{Ti}$ angle to approximately the experimental value. The resulting magnetic moment, downsized by spin-orbit interaction effect, results in good agreement with the measured value, but the calculated band gap is dramatically wrong, about 2.7 eV, against the measured value of 0.1 eV.[7] The results of Ref. 72 go to the opposite direction: the magnetic ground state remains wrong even upon inclusion of correlation effects, but the band gap, 0.6 eV, is in much better agreement with experiment. A similar trend is also observed for $LaVO_3$.

Hybrid functionals[41,64,67,82,86–89,97–99]: An alternative methodology to DFT and HF which has attracted a considerable attention in the solid-state physics and chemistry communities in the last two decades is the so-called hybrid functional approach. Originally introduced by Becke in 1993,[49] the hybrid functional scheme relies on a suitable mixing between HF and *local*/*semilocal* (LDA/GGA) DFT theories, in which a portion of the exact *nonlocal* HF exchange

$$E_{\mathrm{X}}^{\mathrm{HF}}(r,r') = -\frac{1}{2}\sum_{i,j}\int\int d^3\mathbf{r}\, d^3\mathbf{r}' \frac{\phi_i^*(\mathbf{r})\phi_j(\mathbf{r})\phi_j^*(\mathbf{r}')\phi_i(\mathbf{r}')}{|\mathbf{r}-\mathbf{r}'|} \quad (2)$$

is mixed with the complementary LDA/GGA *local/semilocal* approximated exchange $E_{\mathrm{X}}^{\mathrm{DFT}}(r)$. The resulting general hybrid XC kernel $E_{\mathrm{XC}}^{\mathrm{Hybrid}}$ [decomposed over its exchange (X) and correlation (C) terms] can be written in the form

$$E_{\mathrm{XC}}^{\mathrm{Hybrid}} = \alpha E_{\mathrm{X}}^{\mathrm{HF}} + (1-\alpha)E_{\mathrm{X}}^{\mathrm{LDA/GGA}} + E_{\mathrm{C}}^{\mathrm{LDA/GGA}}, \quad (3)$$

where the mixing factor α controls the amount of exact $E_{\mathrm{X}}^{\mathrm{HF}}$ incorporated in the hybrid functional. Similarly to DFT + U (which makes use of the HF–type intra-atomic interaction U, as recalled above), hybrid functionals tend to correct the LDA/GGA delocalization error and to provide a better description of TMO with partially filled d and f states. The advantages with respect to DFT + U is that hybrid functionals (i) do not suffer from the double-counting term [see Eq. (1)] and, even most importantly, (ii) use an orbital-dependent functional acting on all states, extended as well as localized (in the DFT + U method, the improved treatment of exchange effects is limited to states localized inside the atomic spheres, and usually limited to the partially filled TM shell). Although both schemes problematically depend on *semiempirical* parameters such as U and J in DFT + U and the mixing factor α in hybrid functionals, many attempts have been made to overcome these difficulties.[100–106]

Although sparse in literature, hybrid functionals studies of LaMO_3 are increasing in the last few years.[41,64,67,82,86,87,89,107–109] Applications of the renowned Becke, three-parameter, Lee-Yang-Parr B3LYP functional[49] to $LaMnO_3$ (Refs. 64,67, and 87) have shown that this method properly favors the type-A AFM ground state and provides an accurate description of the band gap, magnetic coupling constants, and Gibbs formation energies. The only structural optimization of the JT distorted structure, however, delivers lattice constants which deviate by 5% from experiment.[87] We have recently reported that HSE performs very well in predicting the ground-state properties of $LaMnO_3$, including the optimized structural parameters, and that the data are slightly dependent on the actual value of the mixing factor.[41,89] Gryaznov *et al.* have successfully studied the structural and phonon properties of $LaCoO_3$ using the PBE0 (Perdew-Ernzerhof-Burke)[110] hybrid functional and reported a substantial improvement with respect to conventional DFT. The application of HSE and PBE0 functionals to $LaNiO_3$, conversely, turned out to give poor agreement with the experimental photoemission spectroscopy (PES); this is in line with precedent unsatisfactory HSE/PBE0 results obtained for other itinerant magnetic metals.[111] The influence of the nonlocal exchange on the electronic properties of $LaTiO_3$ has been investigated recently by Iori and co-workers.[109] By adopting the experimental structure, these authors clarified that the improved description of HSE over DFT + U is due to a correct repositioning of the O p states, and show that by fixing the mixing parameter α to its "standard" value 0.25, the band gap and the magnetic moment are significantly overestimated with respect to measurements.

SIC (Refs. 112 and 113): Another approach to correct the self-interaction (SI) LDA/GGA problem is the self-interaction correction method[45–48] in which an approximated (atomiclike and orbitally averaged) self-interaction is subtracted from the LDA XC functional. Although conceptually different from LDA + U (in LDA + U an additional effective Coulomb term is added to the LDA/GGA functional), the SIC method is often pragmatically viewed as a generalized LDA + U approach in which the atomic SI plays the role of the U.[112] Several implementations of the SIC scheme have been proposed, characterized by a different level of complexity in treating the SI term and from the different underlying computational framework,[45–48] but all demonstrated an appreciable accuracy in predicting and interpreting the electronic structure of a vast range of systems, including SCSs and TMOs.[114]

A valid illustration of the performance of the SIC method is supplied by the results obtained for $LaTiO_3$ recently discussed by Filippetti *et al.*[112] By assuming the experimental cell parameters, SIC finds the correct AFM type-G insulating ordering and delivers internal structural distortions close to the experimental ones. As a downside, however, the magnitudes of the band gap (1.6 eV) and magnetic moment (0.89 μ_{B}) are substantially larger than the corresponding measured values (≈0.2 eV and ≈0.5 μ_{B}, respectively). Other SIC applications to the LaMO_3 series are limited, to our knowledge, to the ideal undistorted cubic phase of $LaMnO_3$,[113] for which a stringent comparison with experiment is difficult to do.

GW (Refs. 41,76, and 78): We finally recall the main achievements on LaMO_3 acquired using the GW approximation, a computational method fundamentally different from both DFT and HF. GW is configured to reflect and to treat the quasiparticle nature of electrons on the basis of Green's function many-body perturbation theory[50] by explicitly accounting for the nonlocal and frequency-dependent self-energy (Σ) in a suitably rewritten Schrödinger-type equation. In the GW approximation, Σ is approximated to the lowest-order term of the Hedin's equation, and can be written as

$$\Sigma = iGW, \quad (4)$$

where G is the Green's function and W is the dynamically screened Coulomb kernel. In the most widely used single-shot G_0W_0 approximation, both G and W are treated in an unperturbed manner, but with increasing computer power self-consistent or partially self-consistent GW schemes are becoming more and more possible.[41,115,116] Due to the extensive computing time required to perform GW-like calculations, only few GW data are available in literature for complex systems. Among these, the works of Nohara *et al.*[76,78] represent a very comprehensive example of a systematic application of GW to LaMO_3 starting from preconvergent LDA + U wave functions. These authors have obtained excellent agreement with experimental spectra, but probably due to the uncertainties connected to the choice of U in preparing the initial wave functions, the values of the computed band gaps deviate significantly from the experimental estimations, especially for $LaTiO_3$, $LaVO_3$, and $LaCoO_3$. Good agreement with experiment has been also obtained for $LaMnO_3$ using a partially self-consistent GW_0 approach, in this case starting from the GGA wave function.[41]

The paper is organized as it follows. In Sec. II, we illustrate the computational method and its technical aspects; in Sec. III, we report the results on the structural optimization (Sec. III A) and electronic and magnetic properties (Sec. III B). A more general discussion on the observed trends and behaviors is developed in Sec. IV, and finally in Sec. V, we draw our summary and conclusions.

II. COMPUTATIONAL ASPECTS

All calculations were performed using the Vienna *ab initio* simulation package[117,118] (VASP) employing DFT and hybrid-DFT approaches within the projector augmented wave method[119,120] and the PBE parametrization scheme[93] for the XC functional. In the screened hybrid-DFT HSE approach adopted in this study, part of the short-range (sr) PBE exchange functional is replaced by an equal portion of exact HF exchange, according to the general prescription

$$E_{\mathrm{XC}}^{\mathrm{HSE}} = \alpha E_{\mathrm{X}}^{\mathrm{HF,sr},\mu} + (1-\alpha) E_{\mathrm{X}}^{\mathrm{PBE,sr},\mu} + E_{\mathrm{X}}^{\mathrm{PBE,lr},\mu} + E_{\mathrm{C}}^{\mathrm{PBE}}, \tag{5}$$

where μ controls the range separation between the sr and long-range (lr) parts of the Coulomb kernel ($1/r$, with $r = |\mathbf{r} - \mathbf{r}'|$), decomposed over long (L) and short (S) terms:

$$\frac{1}{r} = S_\mu(r) + L_\mu(r) = \frac{\mathrm{erfc}(\mu r)}{r} + \frac{\mathrm{erf}(\mu r)}{r}. \tag{6}$$

The reason to include a screening parameter μ is motivated by the computational effort required in computing the spatial decay of the HF X interaction. In the refined HSE06 hybrid functional, μ is set equal to 0.20 Å^{-1} which corresponds to the distance $2/\mu$ at which the HF X interactions start to become negligible. For $\mu = 0$, the PBE0 functional is recovered,[110] whereas for $\mu \to \infty$, HSE becomes identical to PBE. Aside from the computational cost, the main beneficial consequence of the inclusion of a screening strategy in PBE0 is that screened hybrids can give access to the metallic state, which is unaffordable by unscreened PBE0-like hybrids. The HSE method has proven to improve the quantitative and qualitative prediction of a large variety of materials, including conventional semiconductors,[121,122] transition-metal oxides,[123–125] ferroelectrics,[126] and surfaces.[127,128] The mixing parameter α, determining the amount of exact nonlocal HF X included in the hybrid XC functional, is usually set to 0.25.[52] In this HSE case, the PBE functional is recovered for $\alpha = 0$.

Thus, the HSE06 depends by construction on two parameters, μ and α. Although their standard values are routinely used in solid-state calculations, it is to be expected that they may vary from material to material[106,129] or that they may be property dependent.[64,130,131] Unfortunately, a rigorous first-principles procedure to determine the choice of these parameters does not exist. The conventional value $\alpha = \frac{1}{4}$ is determined by perturbation theory.[110] The choice $\mu = 0.20$ Å^{-1} has proven to be a practical compromise between computational cost and quality of the results.[132] Considering that most of the tests and fitting procedures have been performed taking as a reference atomic or molecular energetical and structural properties, the direct acquisition of these standard values in an extended solid-state system is not straightforward.[110,132]

By linking hybrid density functional theory with many-electron XC self-energy Σ within a GW framework, it has been proposed that the mixing factor α can be interpreted as the inverse of the dielectric constant ϵ_∞.[129,133–135] Based on this idea, an approximated recipe to determine the *optimum* value of α can be obtained:

$$\alpha_{\mathrm{opt}} \approx \frac{1}{\epsilon_\infty}, \tag{7}$$

which depends solely on the dielectric constant and on the "unknown" factor of proportionality. It is important to emphasize that this relation should be interpreted as an *a posteriori* justification of the choice of the optimum value of α, and not as a fundamental quantum mechanical definition of the mixing factor. It follows straightforwardly that for metal ($\epsilon_\infty = \infty$), α_{opt} is equal to zero. Several limitations affect this practical rule and degrade its *ab initio*nature,[135] above all an accurate calculation of the dielectric constant, which is presently very difficult in particular for complex TMOs.

Following this line of thought, other strategies have been introduced to overcome this problem invoking density functional estimators[136] in the spirit of the Tran and Blaha functional,[137] which furnishes parametric expressions inevitably dependent on the specific material data set, usually limited to monoatomic and binary semiconductors.[106] To complicate the situation even further, there is some amount of arbitrariness in transferring the $\alpha_{\mathrm{opt}} \approx \frac{1}{\epsilon_\infty}$ relation from unscreened PBE0-like hybrids to screened ones like HSE, where screening is already present in some form in the range separation controlled by the screening factor μ. These complications become particularly cumbersome when one moves from "standard" monoatomic and binary semiconductors to the more complex ternary TM perovskites. As a matter of fact, due to the absence of a systematic study on the influence of α in this class of compounds, the large majority of hybrid functionals studies on ternary TMOs have been performed using the standard $\frac{1}{4}$ compromise, although there are neither fundamental nor practical justifications for this choice.

Thus, in order to shed some light on the role of α in a representative class of ternary TMOs with a largely varying degree of screening and competition between localization/delocalization effects, we have performed our HSE calculations using four different values of α: (i) low mixing (strong screening): 0.10 (HSE-10), 0.15 (HSE-15), (ii) standard mixing: 0.25 (HSE-25), and (iii) high mixing (low screening): 0.35 (HSE-35). The careful analysis of structural, electronic, and magnetic properties will allow us to draw some general trends which should serve as a guidance for future HSE applications.

Technical setup. The plane-wave cutoff energy was set to 300 eV. $4\times4\times4$, $6\times6\times6$, and $8\times8\times8$ Monkhorst-Pack k-point grids were used to sample the Brillouin zones for $P_{nma}/P_{2_1/b}$, $R_{\bar{3}c}$, and $P_{4/m}$ structures, respectively. Structural optimization was achieved by relaxing the volume, lattice parameters, lattice angles, and internal atomic positions throughout the minimization of the stress tensor and forces using standard convergence criteria. Finally, the dielectric constant ϵ_∞ was computed adopting the perturbation expansion after discretization (PEAD) method.[116,138]

III. RESULTS

This section is subdivided into two parts which are devoted to the presentation of the structural (Sec. III A), and electronic and magnetic (Sec. III B) properties, respectively. In each section, we will summarize the specific results obtained for each member of the LaMO$_3$ series, and in the next section (Sec. IV) we will provide a more reasoned discussion on the general trends observed across the series.

As anticipated in the Introduction, hybrid functionals can be simplistically viewed as an orbital-dependent DFT + U approach in which the onsite electron-electron interaction parameter U is replaced by the parametric inclusion of a portion of the exact HF exchange quantified by the mixing factor α. In DFT + U calculations, the U is usually either tuned to fit some specific physical property (i.e., band gap, magnetic moment, volume, etc.), or calculated within constrained-LDA procedures.[100–104] In contrast, most of the available HSE-based calculations present in literature are done at fixed mixing parameter $\alpha = 0.25$. This might erroneously convey the idea of a minor role played by the mixing factor or, even more fundamentally misleading, that HSE is a purely *ab initio* (i.e., parameter-free) scheme. As already discussed previously, in the last few years the modeling community has started to address this issue,[64,106,129] but the amount of available data are still very limited, in particular for complex oxide. It is therefore instructive to briefly recall a few results on the choice of the U in DFT + U studies of transition-metal oxides in order to possibly formulate some expectations on the behavior of the mixing parameter α in HSE. A good example to start with is transition-metal monoxides (TMOs: MnO, FeO, CoO, and NiO), where the TM possesses the oxidation state 2+ (M^{2+}). Several LDA + U studies have shown that a U between 6 and 8 eV can provide an accurate enough prediction of band gaps for all TMOs.[44,139] Going from M^{2+} to M^{3+}, the number of the localized electrons decreases. Thus, it might be expected that the magnitude of the Coulomb interaction increases due to the contraction of the spatial extension of the of the 3d (M^{3+}) wave functions.[140] However, by comparing M^{2+}O and LaM^{3+}O$_3$ photoemission data, it can be unambiguously concluded that the effective Coulomb interaction decreases in M^{3+} compounds.[140–145]

Under the assumption that in LaM^{3+}O$_3$ the t_{2g} electrons are localized and the e_g electrons are itinerant, Solovyev[55] has explained this apparent contradiction by invoking the strong screening associated with the e_g electrons. Indeed, the computed value of U for the t_{2g} shell in LaM^{3+}O$_3$ is significantly reduced with respect to U for the d states in M^{2+}O. The strength of the screening depends on the filling of the e_g orbital: it is strong at half-filling and less efficient when the e_g are nearly empty or occupied. The results of Solovyev indicate that this t_{2g}-U approach reproduces sufficiently well the main features of early (Ti-V-Cr) and late (Co-Ni) LaMO$_3$ compounds but fails for LaFeO$_3$ (much too small band gap and magnetic moment) and LaMnO$_3$ (small gap). Clearly, effects other than e_g itinerancy contribute to the strength of the U, such as the screening from non-3d electrons, M(3d/4s)-O(2p) hybridization, and lattice relaxation which can explain the discrepancy between self-consistent +U methods and experiments.

A fitting-U approach can selectively adjust the comparison with the experimental gap (not for LaCrO$_3$) at the expense of a rigorous description of the position of the e_g, t_{2g}, and O(p) subbands (i.e., the "correct" value of the band gap can arise from a fundamentally incorrect artificial electronic structure). This failure prevents any physically sound specification/understanding of the (MH or CT) character of the gap: in Ref. 59, for instance, the gap of LaMnO$_3$ is found to be predominantly CT like, in discrepancy with the actual situation (LaMnO$_3$ is a MH insulator with a gap opened between occupied and empty e_g states, partially hybridized with O p states). Furthermore, the "optimum" U's resulting from fitting-U schemes do not seem to reflect the observed M^{2+} to M^{3+} U reduction, which is an additional sign of the inadequacy of such a procedure.

Considering that standard HSE ($\alpha = 0.25$) performs quite well for TM monoxides,[123,146] we can expect that a smaller value will turn out to be more appropriate for reproducing the ground-state properties of LaMO$_3$. Furthermore, given the full-orbital character of HSE we may expect that hybridization effects and screening from non-3d electrons will be better described as compared to DFT + U. Finally, we should point out that the choice to perform a complete structural optimization at each considered value of α allows for a more genuine account of the structural contribution to the screening which is disguised in frozen-lattice (atomic positions fixed to experimental ones) calculations.

A. Structural properties

As already mentioned in the Introduction, four different crystal symmetries are encountered across the LaMO$_3$ series (see Fig. 2): (i) orthorhombic P_{nma} for LaScO$_3$, LaTiO$_3$, LaCrO$_3$, LaMnO$_3$, and LaFeO$_3$; (ii) monoclinic $P_{2_1/b}$ for LaVO$_3$; (iii) rhombohedral $R_{\bar{3}c}$ for LaCoO$_3$ and LaNiO$_3$; and (iv) tetragonal $P_{4/m}$ for LaCuO$_3$. All these different structures share the same octahedral perovskitic building block MO$_6$, characterized by one central TM metal surrounded by two apical (O$_1$) oxygen atoms and four planar (O$_2$) oxygen atoms. Depending on the specific compound, the MO$_6$ octahedra can undergo two kinds of structural distortions: the JT distortion, manifested by a short (s) and long (l) M-O$_2$ in-plane distances and medium (m) M-O$_1$ vertical ones (along the octahedral axis), and the GFO tilting of the $M - \widehat{\mathrm{O}}_1 - M$ and $M - \widehat{\mathrm{O}}_2 - M$ 180° angles. The cooperative JT distortion is usually measured in terms of the JT modes $Q_2 = 2(l - s)/\sqrt{2}$ and $Q_3 = 2(2m - l - s)/\sqrt{6}$. In our full structural relaxation, we have optimized the volume (V), lattice parameters a, b, and c, the monoclinic/rhombohedral angle β, as well as all internal atomic coordinates [this clearly includes all relevant GFO and JT structural parameters $\mathrm{M} - \widehat{\mathrm{O}}_1 - \mathrm{M}$ (θ_1), $M - \widehat{\mathrm{O}}_2 - M$ (θ_2), Q_2, and Q_3].

A graphical summary of the observed trend of the most relevant structural parameters is given in Fig. 3. The progressive reduction of the volume from Sc to Cu is clearly associated with the almost monotonically decrease of the M ionic radius R_M, the size of which is determined by the

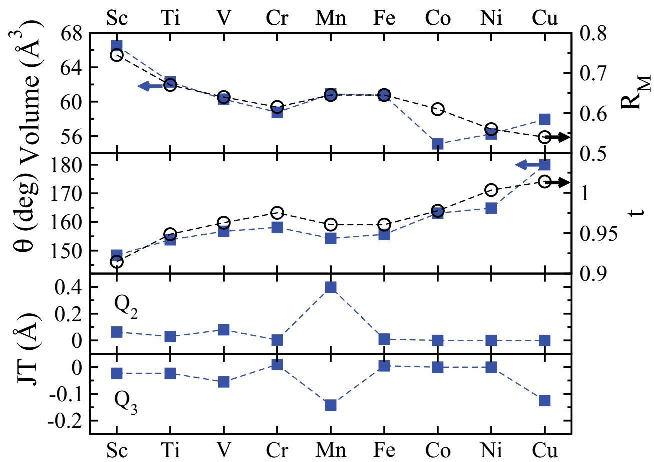

FIG. 3. (Color online) Experimental trend of volume (V), average tilting angle (θ), and JT distortions (Q_2 and Q_3) for the LaMO$_3$ series from M = Sc to Cu. The corresponding trend of the tolerance factor $t = (R_A + R_O)/\sqrt{2}(R_M + R_O)$, and R_M is also shown.

competition between the size of the 4s shell (where extra protons are pulled in) and the additional screening due to the increasing number of 3d electrons: adding protons should lead to a decreased atom size, but this effect is hindered by repulsion of the 3d and, to a lesser extent, 4s electrons. The V/R_M curves show a plateau at about half-filling (Cr-Mn-Fe), indicating that for this trio of elements these two effects are essentially balanced and atom size does not change much. The volume contraction is associated with a rectification of the average $(M - \widehat{O}_1 - M + M - \widehat{O}_2 - M)/2$ tilting angle θ, which follows very well the evolution of the tolerance factor $t = (R_A + R_O)/\sqrt{2}(R_M + R_O)$ (where R_A, R_M, and R_O indicate the ionic radius for La, M = Sc–Cu, and O, respectively). This indicates that the tolerance factor is indeed a good measure of the overall stability and degree of distortion of perovskite compounds. Clearly, the value of t is well within the range of stability set to $0.78 < t < 1.05$. The bottom panel of Fig. 3 conveys the message that Q_2 and Q_3 assume non-negligible values for LaMnO$_3$ only, confirming that JT distortions are predominant in perovskites containing cations such as Cu^{2+} and Mn^{3+} in their octahedral cation site.

In the following sections, we will report on the full structural optimization of LaMO$_3$ at PBE and HSE (for different values of α) and will provide a one-to-one comparison with available experimental data, also in terms of the mean absolute relative error (MARE, not given for the very small quantities Q_2 and Q_3).

1. LaScO$_3$

LaScO$_3$ crystallizes with a P_{nma} orthorhombic structure, and shows the largest tilting instabilities of all LaMO$_3$ series (147.3°).[147] The JT parameters Q_2 and Q_3 are almost zero (0.063 and −0.023, respectively) and, as a consequence, the Sc-O bond-length disproportionation is negligible: both planar and vertical Sc-O bond lengths are all ≈2.1 Å. The computed structural data are collected in Table II. All methods deliver a quite satisfactory description with an overall MARE less than 1%. PBE supplies the best agreement with measurements

TABLE II. Structural data for LaScO$_3$. Comparison between the optimized parameters calculated using PBE and HSE (with different values of the mixing factor) and the available (room-temperature) experimental data taken from Ref. 147. The relative error (in brackets, in %) and the mean absolute relative error (MARE, %) is also supplied.

	Expt.	HSE-35	HSE-25	HSE-15	HSE-10	PBE
V (Å^3)	266.09	262.02	263.48	265.12	265.99	267.90
		(1.5)	(1.0)	(0.4)	(0.0)	(0.7)
a (Å)	5.787	5.764	5.780	5.794	5.798	5.810
		(0.4)	(0.1)	(0.1)	(0.2)	(0.4)
b (Å)	8.098	8.050	8.061	8.076	8.088	8.108
		(0.6)	(0.5)	(0.3)	(0.1)	(0.1)
c (Å)	5.678	5.647	5.655	5.666	5.672	5.686
		(0.5)	(0.4)	(0.2)	(0.1)	(0.1)
Sc-O$_m$ (Å)	2.104	2.091	2.096	2.100	2.103	2.108
		(0.6)	(0.4)	(0.2)	(0.0)	(0.2)
Sc-O$_l$ (Å)	2.140	2.095	2.101	2.108	2.109	2.115
		(2.1)	(1.8)	(1.5)	(1.4)	(1.2)
Sc-O$_s$ (Å)	2.096	2.082	2.086	2.091	2.093	2.098
		(0.7)	(0.5)	(0.2)	(0.1)	(0.1)
θ_1 (°)	148.39	148.42	148.08	148.14	148.19	148.18
		(0.0)	(0.2)	(0.2)	(0.1)	(0.1)
θ_2 (°)	146.29	149.98	149.95	149.55	149.68	149.53
		(2.5)	(2.5)	(2.2)	(2.3)	(2.2)
MARE		1.0	0.8	0.6	0.5	0.6
Q_2	0.063	0.018	0.021	0.024	0.023	0.023
Q_3	−0.023	0.004	0.005	0.000	0.003	0.002

(MARE = 0.5 %). The most critical quantities for theory are Sc-O$_l$ and θ_2, for which relative errors larger than 1% and 2% are found, respectively. We can thus conclude that for an accurate account of the structural properties of LaScO$_3$, it is not required to apply beyond-DFT methods. As we will see in the next section, this is not the case for the electronic properties.

2. LaTiO$_3$

Similarly to LaScO$_3$, the low-temperature space group of LaTiO$_3$ is P_{nma} with small JT distortions due to the low JT activity of the single $t_{2g}^{\uparrow}$ orbital and large GFO distortions caused by the large size difference between Ti and La ions.[148,149] Although the overall PBE MARE is only 1%, the relaxed structure parameters given by HSE functionals are appreciably better (MARE ≈ 0.3%) than PBE, regardless of the amount of exact HF exchange, as summarized in Table III. The PBE errors mostly arise from an incorrect description of the tilting angles, which are by far (≈3%) overestimated with respect to the low-temperature experimental data.[148] As for the volume, PBE furnishes a nice optimized value, which is improved by going to large α HSE setups (HSE-35, HSE-25).

3. LaVO$_3$

LaVO$_3$ is the only member of the LaMO$_3$ series displaying a monoclinic structure with $P_{2_1/b}$ space group.[150] The unit cell contains two inequivalent V sites (V$_1$ and V$_2$), which sit in the center of GFO distorted octahedra not subjected to significant JT distortions. Due to the occurrence of two different V atoms in the unit cell, two different sets of V-O

TABLE III. Structural data for $LaTiO_3$. Comparison between the optimized parameters calculated using PBE and HSE (with different values of the mixing factor) and the available experimental data taken from Ref. 148. The relative error (in brackets, in %) and the mean absolute relative error (MARE, %) is also supplied.

	Expt.	HSE-35	HSE-25	HSE-15	HSE-10	PBE
V (Å^3)	249.17	250.03	250.00	250.98	251.17	250.61
		(0.3)	(0.3)	(0.7)	(0.8)	(0.6)
a (Å)	5.589	5.599	5.597	5.612	5.617	5.646
		(0.2)	(0.1)	(0.4)	(0.5)	(1.0)
b (Å)	7.901	7.931	7.909	7.915	7.913	7.929
		(0.4)	(0.1)	(0.2)	(0.2)	(0.4)
c (Å)	5.643	5.631	5.648	5.651	5.650	5.598
		(0.2)	(0.1)	(0.1)	(0.1)	(0.8)
Ti-O$_s$ (Å)	2.028	2.038	2.034	2.033	2.029	2.018
		(0.5)	(0.3)	(0.2)	(0.0)	(0.5)
Ti-O$_l$ (Å)	2.053	2.059	2.069	2.071	2.068	2.033
		(0.3)	(0.8)	(0.9)	(0.7)	(1.0)
Ti-O$_m$ (Å)	2.032	2.027	2.023	2.028	2.030	2.029
		(0.2)	(0.4)	(0.2)	(0.1)	(0.1)
θ_1 (°)	153.78	153.12	152.98	153.54	154.25	158.47
		(0.4)	(0.5)	(0.2)	(0.3)	(3.0)
θ_2 (°)	152.93	152.64	152.54	152.59	152.97	156.37
		(0.2)	(0.3)	(0.2)	(0.0)	(2.2)
MARE		0.31	0.33	0.35	0.31	1.07
Q_2	0.029	0.046	0.065	0.062	0.054	0.006
Q_3	−0.023	−0.008	−0.021	−0.027	−0.031	−0.021

bond lengths and tilting angle θ_2 (θ_{21} and θ_{22}) are identified. The comparison between the low-temperature experimental data and the theoretical values are collected in Table IV. The general situation is similar to $LaTiO_3$: the PBE MARE, 1%, is about twice larger than the average HSE MARE. The PBE relative errors are large for the tilting angles and V-O bond lengths, but rather small for volume and lattice constants. HSE leads to slightly better data, in particular in the range $0.10 < \alpha < 0.25$, but the volume and lattice constants are reproduced less accurately than at the PBE level.

TABLE IV. Structural data for $LaVO_3$. Comparison between the optimized parameters calculated using PBE and HSE (with different values of the mixing factor) and the available ($T = 10$ K) experimental data taken from Ref. 150. The relative error (in brackets, in %) and the mean absolute relative error (MARE, %) is also supplied.

	Expt.	HSE-35	HSE-25	HSE-15	HSE-10	PBE
V (Å^3)	241.10	240.31	241.33	242.20	242.45	241.64
		(0.3)	(0.1)	(0.5)	(0.6)	(0.2)
a (Å)	5.5917	5.562	5.582	5.622	5.637	5.613
		(0.5)	(0.2)	(0.5)	(0.8)	(0.4)
b (Å)	7.7516	7.801	7.787	7.729	7.713	7.729
		(0.6)	(0.5)	(0.3)	(0.5)	(0.3)
c (Å)	5.5623	5.538	5.552	5.574	5.577	5.570
		(0.4)	(0.2)	(0.2)	(0.3)	(0.1)
β (°)	90.13	89.93	90.16	90.16	90.18	90.03
		(0.2)	(0.0)	(0.0)	(0.1)	(0.1)
V$_2$-O$_s$ (Å)	1.979	2.019	1.993	1.974	1.966	1.962
		(2.0)	(0.7)	(0.3)	(0.7)	(0.9)
V$_2$-O$_l$ (Å)	2.039	2.007	2.019	2.055	2.054	2.012
		(1.6)	(1.0)	(0.8)	(0.7)	(1.3)
V$_2$-O$_s$ (Å)	1.979	2.004	1.999	1.984	1.991	2.011
		(1.3)	(1.0)	(0.3)	(0.6)	(1.6)
V$_1$-O$_s$ (Å)	1.978	1.969	1.989	1.972	1.965	1.961
		(0.5)	(0.6)	(0.3)	(0.7)	(0.9)
V$_1$-O$_l$ (Å)	2.042	2.007	2.026	2.063	2.059	2.013
		(1.7)	(0.8)	(1.0)	(0.8)	(1.4)
V$_1$-O$_m$ (Å)	1.989	1.997	1.997	1.982	1.990	2.013
		(0.4)	(0.4)	(0.4)	(0.1)	(1.2)
θ_1 (°)	156.74	155.83	155.88	156.65	157.70	160.15
		(0.6)	(0.5)	(0.1)	(0.6)	(2.2)
θ_{21} (°)	157.83	156.23	156.90	157.05	157.06	158.76
		(1.0)	(0.6)	(0.5)	(0.5)	(0.6)
θ_{21} (°)	156.12	157.08	156.23	156.28	156.51	158.26
		(0.6)	(0.1)	(0.1)	(0.2)	(1.4)
MARE		0.82	0.48	0.35	0.51	0.98
Q_{21}	0.085	0.003	0.028	0.101	0.088	0.001
Q_{31}	−0.050	0.023	−0.027	−0.075	−0.093	−0.080
Q_{22}	0.074	0.015	0.042	0.114	0.098	0.002
Q_{32}	−0.060	−0.054	−0.037	−0.082	−0.097	−0.084

4. $LaCrO_3$

The structural data for P_{nma} $LaCrO_3$ are collected in Table V. The full threefold-degenerate t_{2g} shell inhibits completely any tendency to JT distortions but the size difference between La and Cr drives a substantial GFO-like tilting of the CrO_6 octahedra. Also, in this case PBE performs as well as HSE-10 and HSE-15 (MARE = 0.6 %). The overall MARE is further reduced to 0.3% for larger values of α (HSE-25 and HSE-35).

5. $LaMnO_3$

$LaMnO_3$ is the most critical case across the LaMO$_3$ series due to the concomitant occurrence of both GFO and JT structural distortions, the latter originating by the intrinsic instabilities associated with the orbital degeneracy in the e_g channel of the Mn^{3+} cation. The lattice constants and atom positions of O-P_{nma} $LaMnO_3$ were fully optimized at both the PBE and HSE levels within an AFM-A magnetic ordering, though, as we will discuss in the next section, PBE is not able to catch the correct magnetic ground state and rather favors an FM arrangement. The results are listed in Table VI. In this case, PBE does not supply a satisfactory account of the structural properties, reflected by a quite large MARE (≈2%), significantly larger than the corresponding HSE-10 (1.22), HSE-15 (0.81), HSE-25 (0.66), and HSE-35 (0.52). The major obstacle for PBE is the correct prediction of the JT distortions: (i) the relative error for the M-O bond-length disproportionation is as high as 5.5%, and (ii) Q_2 and Q_3 are found to be one third of the measured values. The serious underestimation of Q_2 and Q_3 at PBE level has important consequences on the electronic properties; we will discuss this issue in the next section. We can anticipate that the deficient treatment of Q_2 and Q_3 prevents the opening of the band gap, thereby leading to a metallic solution. HSE-10 improves the estimations of Q_2 and Q_3 with respect to PBE, and with increasing α the MARE get progressively reduced down to 0.52 for $\alpha = 0.35$. The inaccuracy of local functional

TABLE V. Structural data for $LaCrO_3$. Comparison between the optimized parameters calculated using PBE and HSE (with different values of the mixing factor) and the available (room-temperature) experimental data taken from Ref. 151 (similar structural data can be found in Refs. 152 and 153). The relative error (in brackets, in %) and the mean absolute relative error (MARE, %) is also supplied.

	Expt.	HSE-35	HSE-25	HSE-15	HSE-10	PBE
V (Å^3)	235.02	233.45	234.74	236.13	236.69	237.70
		(0.7)	(0.1)	(0.5)	(0.7)	(1.1)
a (Å)	5.483	5.478	5.509	5.494	5.531	5.512
		(0.1)	(0.5)	(0.2)	(0.9)	(0.5)
b (Å)	7.765	7.752	7.766	7.776	7.785	7.795
		(0.2)	(0.0)	(0.1)	(0.3)	(0.4)
c (Å)	5.520	5.498	5.487	5.527	5.531	5.533
		(0.4)	(0.6)	(0.1)	(0.2)	(0.2)
Cr-O_l (Å)	1.977	1.973	1.977	1.982	1.984	1.983
		(0.2)	(0.0)	(0.3)	(0.4)	(0.3)
Cr-O_m (Å)	1.972	1.971	1.975	1.979	1.981	1.985
		(0.1)	(0.2)	(0.4)	(0.5)	(0.7)
Cr-O_s (Å)	1.970	1.970	1.975	1.979	1.980	1.984
		(0.0)	(0.3)	(0.5)	(0.5)	(0.7)
θ_1 (°)	158.14	158.29	158.10	159.76	157.71	158.51
		(0.1)	(0.0)	(1.0)	(0.3)	(0.2)
θ_2 (°)	161.32	159.72	159.60	157.66	159.73	159.30
		(1.0)	(1.1)	(2.3)	(1.0)	(1.3)
MARE		0.30	0.30	0.60	0.51	0.61
Q_2	0.003	0.001	0.001	0.000	0.001	0.001
Q_3	0.010	0.004	0.004	0.004	0.005	−0.002

TABLE VI. Structural data for $LaMnO_3$. Comparison between the optimized parameters calculated using PBE and HSE (with different values of the mixing factor) and the available ($T = 4.2$ K) experimental data taken from Ref. 154. The relative error (in brackets, in %) and the mean absolute relative error (MARE, %) is also supplied.

	Expt.	HSE-35	HSE-25	HSE-15	HSE-10	PBE
V (Å^3)	243.57	243.98	245.82	247.36	244.24	244.21
		(0.2)	(0.9)	(1.6)	(0.3)	(0.3)
a (Å)	5.532	5.526	5.537	5.553	5.661	5.569
		(0.1)	(0.1)	(0.4)	(2.3)	(0.7)
b (Å)	5.742	5.789	5.817	5.820	5.594	5.627
		(0.8)	(1.3)	(1.4)	(2.6)	(2.0)
c (Å)	7.668	7.628	7.633	7.653	7.712	7.793
		(0.5)	(0.5)	(0.2)	(0.6)	(1.6)
Mn-O_m (Å)	1.957	1.954	1.957	1.962	1.979	1.992
		(0.2)	(0.0)	(0.3)	(1.1)	(1.8)
Mn-O_l (Å)	2.184	2.204	2.214	2.213	2.134	2.063
		(0.9)	(1.4)	(1.3)	(2.3)	(5.5)
Mn-O_s (Å)	1.903	1.899	1.905	1.914	1.923	1.971
		(0.2)	(0.1)	(0.6)	(1.1)	(3.6)
θ_1 (°)	154.3	154.78	154.35	154.36	153.96	155.85
		(0.3)	(0.0)	(0.0)	(0.2)	(1.0)
θ_2 (°)	156.7	154.38	154.08	154.17	157.59	157.71
		(1.5)	(1.7)	(1.6)	(0.6)	(0.6)
MARE		0.52	0.66	0.81	1.22	1.90
Q_2	0.398	0.431	0.437	0.423	0.298	0.131
Q_3	−0.142	−0.159	−0.167	−0.165	−0.080	−0.041

TABLE VII. Structural data for $LaFeO_3$. Comparison between the optimized parameters calculated using PBE and HSE (with different values of the mixing factor) and the available (room-temperature) experimental data taken from Ref. 155. The relative error (in brackets, in %) and the mean absolute relative error (MARE, %) is also supplied.

	Expt.	HSE-35	HSE-25	HSE-15	HSE-10	PBE
V (Å^3)	242.90	240.39	242.08	244.02	245.09	246.47
		(1.0)	(0.3)	(0.5)	(0.9)	(1.5)
a (Å)	5.565	5.530	5.569	5.587	5.557	5.618
		(0.6)	(0.1)	(0.4)	(0.1)	(1.0)
b (Å)	7.854	7.829	7.842	7.861	7.868	7.878
		(0.3)	(0.2)	(0.1)	(0.2)	(0.3)
c (Å)	5.557	5.553	5.543	5.556	5.605	5.568
		(0.1)	(0.3)	(0.0)	(0.9)	(0.2)
Fe-O_l (Å)	2.009	2.001	2.006	2.012	2.015	2.018
		(0.4)	(0.1)	(0.1)	(0.3)	(0.4)
Fe-O_l (Å)	2.009	2.002	2.010	2.017	2.024	2.032
		(0.3)	(0.0)	(0.4)	(0.7)	(1.1)
Fe-O_s (Å)	2.002	1.995	2.002	2.008	2.013	2.018
		(0.3)	(0.0)	(0.3)	(0.5)	(0.8)
θ_1 (°)	155.66	155.95	155.52	155.16	155.07	154.83
		(0.2)	(0.1)	(0.3)	(0.4)	(0.5)
θ_2 (°)	157.26	157.10	156.69	156.29	155.78	155.21
		(0.1)	(0.4)	(0.6)	(0.9)	(1.3)
MARE		0.38	0.16	0.30	0.56	0.79
Q_2	0.010	0.010	0.011	0.013	0.016	0.020
Q_3	0.005	0.004	0.000	−0.001	−0.006	−0.011

in reproducing the JT distortions was recently overviewed by Hashimoto *et al.*[83] In particular, these authors have pointed out that DFT $+ U$ can only supply a semiquantitative account of JT changes if the structure is fully relaxed (including volume). This is also valid for purely unrestricted HF approaches. All other non-JT related quantities are equally well described by both methodologies, with relative error generally smaller than 1%, apart from the tilting angles which suffer of slightly larger deviations (1%–1.5%).

6. $LaFeO_3$

The crystal of $LaFeO_3$ is orthorhombic with P_{nma} space group.[155] In the high-spin Fe^{3+} configuration $t_{2g}{}^{\uparrow\uparrow\uparrow}e_g{}^{\uparrow\uparrow}$, the JT distortions are completely suppressed. The optimized structural data, collected in Table VII, show that PBE overestimates the volume by 1.5% but describes well all other parameters, leading to a relatively small MARE of 0.79%. HSE predicts a better volume, especially for α equal to 0.15 and 0.25, but in general HSE improves only marginally the PBE results.

7. $LaCoO_3$

At low temperature, $LaCoO_3$ possesses a slightly GFO-distorted perovskite structure with rhombohedral symmetry ($R_{\bar{3}c}$ space group),[156,157] characterized by a rhombohedral angle of 60.99° (see Fig. 2). The structural data are given in Table VIII. The best agreement with experiment is achieved by HSE-15, but also HSE-10 and HSE-25 lead to relative errors $\leqslant 1\%$. The HSE-25 set of data are in good agreement with previous PBE0 results.[82] PBE performs not bad (MARE

TABLE VIII. Structural data for $LaCoO_3$. Comparison between the optimized parameters calculated using PBE and HSE (with different values of the mixing factor) and the available ($T = 4$ K) experimental data taken from Ref. 157 (room-temperature data can be found in Ref. 158). The relative error (in brackets, in %) and the mean absolute relative error (MARE, %) is also supplied. Here, $\theta_1 = \mathrm{O} - \hat{\mathrm{Co}} - \mathrm{O}$ and $\theta_2 = \hat{\mathrm{Co}} - \mathrm{O} - \mathrm{Co}$. For $LaCoO_3$, we have optimized the structure using a reduced 0.05 mixing parameter and obtained the following data: V = 111.87 (Å^3) (1.5), a = 5.354 (Å) (0.2), Co-O$_1$ = 1.940 (Å) (0.8), O-Co-O = 88.07 (°) (0.5), and Co-O-Co = 161.00 (°) (1.3); MARE = 0.82.

	Expt.	HSE-35	HSE-25	HSE-15	HSE-10	PBE
V (Å^3)	110.17	107.78	109.02	110.39	111.09	114.11
		(2.2)	(1.0)	(0.2)	(0.8)	(3.6)
a (Å)	5.342	5.314	5.328	5.343	5.348	5.405
		(0.5)	(0.3)	(0.0)	(0.1)	(1.2)
β (°)	60.99	60.70	60.87	61.05	61.20	60.99
		(0.5)	(0.2)	(0.1)	(0.3)	(0.0)
Co-O (Å)	1.924	1.904	1.915	1.925	1.932	1.948
		(1.0)	(0.5)	(0.1)	(0.4)	(1.2)
θ_1 (°)	88.55	88.96	88.72	88.49	88.27	88.50
		(0.5)	(0.2)	(0.1)	(0.3)	(0.1)
θ_2 (°)	163.08	165.56	164.06	162.88	161.82	162.45
		(1.5)	(0.6)	(0.1)	(0.8)	(0.4)
MARE		0.95	0.42	0.09	0.44	0.92

below 1%), but overestimates too much the volume (+3.5% with respect to experiment).

8. *$LaNiO_3$*

$LaNiO_3$ crystallizes with a rhombohedral structure with moderate GFO-like distortions.[159] The fully optimized structural parameters are listed in Table IX. Similarly to the isostructural $LaCoO_3$, also in this case PBE gives a large volume (+2.4%), but all other structural quantities are well reproduced (our data are in line with the previous calculation of Guo *et al.*[86]). Within HSE, the larger the amount of HF exchange is included, the more the MARE is reduced: from 0.84% (HSE-10) down to 0.1% (HSE-35).

TABLE IX. Structural data for $LaNiO_3$. Comparison between the optimized parameters calculated using PBE and HSE (with different values of the mixing factor) and the available ($T = 1.5$ K) experimental data taken from Ref. 159. Here, $\theta_1 = \mathrm{O} - \hat{\mathrm{Ni}} - \mathrm{O}$ and $\theta_2 = \mathrm{Ni} - \hat{\mathrm{O}} - \mathrm{Ni}$. The relative error (in brackets, in %) and the mean absolute relative error (MARE, %) is also supplied.

	Expt.	HSE-35	HSE-25	HSE-15	HSE-10	PBE
V (Å^3)	112.48	112.02	112.47	113.42	113.83	115.20
		(0.4)	(0.0)	(0.8)	(1.2)	(2.4)
a (Å)	5.384	5.377	5.380	5.393	5.392	5.415
		(0.1)	(0.1)	(0.2)	(0.1)	(0.6)
β (°)	60.86	60.85	60.95	61.01	60.21	61.16
		(0.0)	(0.1)	(0.2)	(1.1)	(0.5)
Ni-O (Å)	1.933	1.930	1.935	1.941	1.947	1.953
		(0.2)	(0.1)	(0.4)	(0.7)	(1.0)
θ_1 (°)	88.78	88.78	88.63	88.55	88.30	88.41
		(0.0)	(0.2)	(0.3)	(0.5)	(0.4)
θ_2 (°)	64.82	164.79	163.77	163.43	162.12	163.02
		(0.0)	(0.6)	(0.8)	(1.6)	(1.1)
MARE		0.10	0.19	0.43	0.84	0.92

TABLE X. Structural data for $LaCuO_3$. Comparison between the optimized parameters calculated using PBE and HSE (with different values of the mixing factor) and available (room-temperature) experimental data taken from Ref. 161. The relative error (in brackets, in %) and the mean absolute relative error (MARE, %) is also supplied.

	Expt.	HSE-35	HSE-25	HSE-15	HSE-10	PBE
V (Å^3)	57.94	56.07	56.38	57.05	57.28	57.85
		(3.2)	(2.7)	(1.5)	(1.1)	(0.2)
a (Å)	3.819	3.821	3.832	3.844	3.850	3.867
		(0.1)	(0.3)	(0.7)	(0.8)	(1.3)
c (Å)	3.973	3.840	3.840	3.861	3.865	3.869
		(3.3)	(3.3)	(2.8)	(2.7)	(2.6)
Cu-O$_l$ (Å)	1.986	1.920	1.920	1.930	1.933	1.934
		(3.3)	(3.3)	(2.8)	(2.7)	(2.6)
Cu-O$_s$ (Å)	1.909	1.911	1.916	1.922	1.925	1.934
		(0.1)	(0.4)	(0.7)	(0.8)	(1.3)
MARE		2.01	2.01	1.70	1.64	1.59
Q_2						
Q_3	0.125	0.016	0.007	0.014	0.013	0.002

9. *$LaCuO_3$*

$LaCuO_3$ is the only member of the LaMO$_3$ family displaying a tetragonal structure ($P_{4/m}$), which can be suitably tuned to a rhombohedral one under different oxygen pressure conditions.[160] In this paper, we only examine the tetragonal phase. The small elongation of the CuO_6 octahedron associated with the tetragonal form induces a local JT-type distortion, manifested by four equatorial Cu-O bonds close to 1.909 Å and two apical bonds to 1.986 Å. The relaxed structure parameters are shown in Table X. From the structural data it is clear that $LaCuO_3$ represents the most challenging compound of the whole series for both level of theory, with MARE well above 1%. PBE provides the overall best agreement with experiment (MARE = 1.59%), but produces an almost cubic structure, dissimilar from the observed tetragonal one. Hybrid functionals open up a small structural disproportionation between long and short Cu-O bond lengths which is however insufficient to stabilize a well-defined tetragonal form: the lattice parameter c is still very badly accounted for (relative error of about 3%).

10. *Concluding remarks*

Summing up the results presented in this section, we can draw the following conclusions. In general, the structural properties of the LaMO$_3$ series are sufficiently well described by standard PBE, which gives an overall MARE smaller than 1%, with the exceptions of (i) $LaMnO_3$: HSE is essential to treat correctly the JT distortions which are a crucial ingredient to find and explain the A-AFM ordered insulating orbitally ordered state. (ii) $LaCuO_3$: neither PBE nor HSE are capable to deliver MARE smaller than 1.5%. The amount of nonlocal HF exchange does not have a decisive and univocal effect on the structural properties apart for the d^0-band insulator

$LaScO_3$ for which the results get worse with increasing α. In all other cases, an improvement over PBE results is obtained for all values of α tested in this study, and the standard 0.25 compromise seems to appear a reasonable choice. This was already noted for the case of actinide dioxides for which the standard value of α yields to excellent volumes.[34] However, as we will discuss in the next section, with this value of α the band gaps are found to be exceedingly overestimated with respect to the measured ones.

B. Electronic structures and magnetic properties

The focus of this section is the presentation of the electronic [density of states (DOS), band structures, and band gaps] and magnetic (magnetic moment m and magnetic energies for different spin orderings) results for the entire LaMO_3 series, given for both the experimental and the fully optimized structures. We note that from the magnetic energies it is possible to extract an estimation of the magnetic coupling constants by means of a mapping onto an Heisenberg-type spin Hamiltonian.[36,37,41,51,108,125,146,162]

Here, we are particularly interested on the modifications induced in the calculated quantities by the value of the mixing parameter α, from 0 (PBE) to 0.35 (HSE-35). To this aim, following the outline adopted in the previous section, we will sequentially discuss the electronic and magnetic structures case by case. A more general discussion on the evolution of the chemical and physical properties of LaMO_3 perovskites from M = Sc to Cu will be provided in the next section.

1. d^0: $LaScO_3$

$LaScO_3$ is a nonmagnetic band insulator with the d^0 (Sc^{3+}) electronic configuration, and an optically measured band gap of about 6.0 eV opened between the O $2p$ valence band and the Sc $3d$ unoccupied band.[7,163] Our calculations confirm this picture as seen from the density of states shown in Fig. 4, but the band gap value predicted at PBE (3.81 and 3.92 eV for

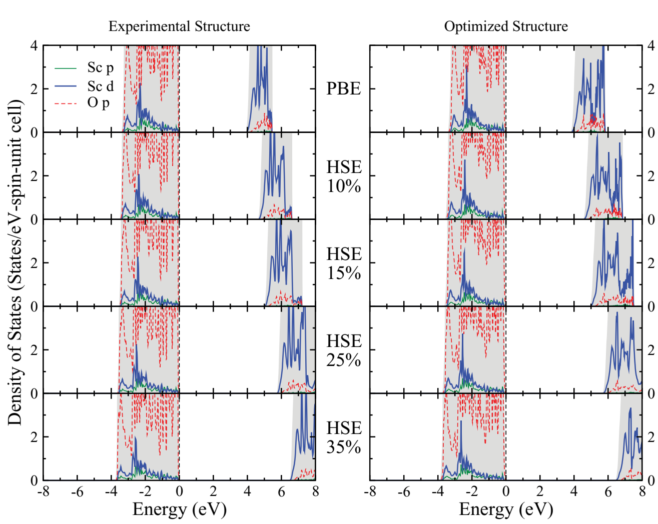

FIG. 4. (Color online) l-projected DOS of nonmagnetic $LaScO_3$ with experimental (left) and relaxed (right) structures based on PBE and HSE (HSE-35, HSE-25, HSE-15, HSE-10) functionals. The shadow area indicates the total DOS.

TABLE XI. The band gap Δ (eV) of $LaScO_3$ calculated within PBE and HSE (HSE-0.10, HSE-15, HSE-25, and HSE-35) using both the experimental and the relaxed structures (see Table II). Other theoretical values are also listed for comparison, along with the experimental measurements.

Theory				
Optimized structure				
HSE-35	HSE-25	HSE-15	HSE-10	PBE
6.495	5.730	4.995	4.635	3.915
Experimental structure				
HSE-35	HSE-25	HSE-15	HSE-10	PBE
6.435	5.685	4.920	4.560	3.810
Other works				
LDA				
3.98[a]				
Experiment				
~6.0[b], 5.7[c]				

[a]Reference 65.
[b]Reference 7.
[c]Reference 163.

the experimental and fully optimized structures, respectively, in agreement with previous calculations[65]) seriously underestimates the experimental value. The HSE data collected in Table XI indicate that the correct value of the gap is recovered by admixing 25% of HF exchange. Clearly, the band gap increases with increasing HF percentage, but the DOS (see Fig. 4) always provides the same qualitative O p/Sc d picture. The band dispersion associated with the 25% choice given in Fig. 5 shows that the band gap is direct and located at Γ, but given the flatness of the topmost occupied bands (O p) and, to a lesser extent, the Sc d bands at about 6 eV, the value of the (direct) band gap does not change much in the entire **k** space. This is in agreement with the experimental optical

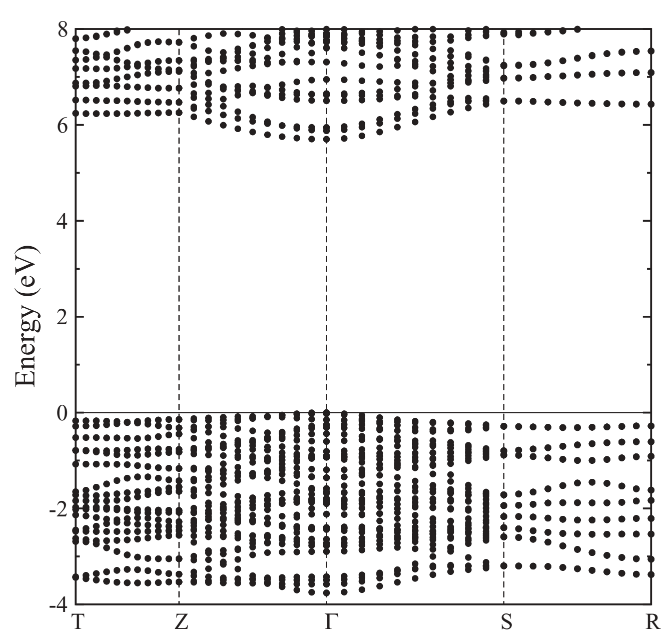

FIG. 5. Band structure of $LaScO_3$ computed at HSE level (α = 0.25) using the optimized structure.

spectra which show a sudden and very intense onset of the optical conductivity at 6 eV.[7]

2. d^1: $LaTiO_3$

$LaTiO_3$ is a G-AFM MH insulator with a magnetic moment of about 0.5 μ_B,[148,164] in which the single 3d electron occupies one Ti t_{2g} orbital. The physics of the orbital degree of freedom has attracted considerable attention.[148,165] This nominal $t_{2g}^{\uparrow}$ configuration gives rise to a distinctive orbitally ordered ground state characterized by a very small band gap of 0.1–0.2 eV,[7,166] which has spurred a lot of theoretical study aiming to clarify the physics underlying this peculiar behavior.[72,112,167–171]

TABLE XII. The band gap Δ (eV), magnetic moment m (μ_B/Ti), magnetic energy (given with respect to the FM energy, in meV) of $LaTiO_3$ calculated by PBE and HSE (HSE-35, HSE-25, HSE-15, HSE-10) using both the experimental and relaxed structures (Table III). The gaps in brackets are for the G-type, which is not the most favorable ordering for $\alpha = 0.10$. Other theoretical values are also listed for comparison, along with the experimental measurements.

	Theory				
			Optimized structure		
	HSE-35	HSE-25	HSE-15	HSE-10	PBE
Δ	2.835	1.815	0.810	0.225 (0.315)	0.000
m	0.908	0.868	0.790	0.707	0.497
A-AFM	−26	−39	−57	−77	−23
C-AFM	−3	−16	0	25	−13
G-AFM	−33	−57	−62	−63	−17
			Experimental structure		
	HSE-35	HSE-25	HSE-15	HSE-10	PBE
Δ	2.700	1.710	0.720	0.165 (0.270)	0.0
m	0.905	0.868	0.789	0.702	0.621
A-AFM	−29	−36	−53	−70	−49
C-AFM	−35	−30	−7	32	−21
G-AFM	−63	−68	−65	−52	−5
			Other works		
	LDA	LDA + U	GW	HF	
Band gap		0.49[a], 0.5[b] 0.4[c], 0.16[d]	1.00[a]	2.7[e],0.6[f]	
m		0.68[a], 0.92[b] 0.52[g], 0.7[c] 0.58[d]	0.68[a]	0.55[e],0.76[f]	
			Experiment		
Δ			0.1[h], 0.2[i]		
m			0.45[j], 0.57[k]		

[a]Reference 78.
[b]Reference 55.
[c]Reference 69.
[d]Reference 74.
[e]Reference 57.
[f]Reference 72.
[g]Reference 79.
[h]Reference 7.
[i]Reference 166.
[j]Reference 172.
[k]Reference 148.

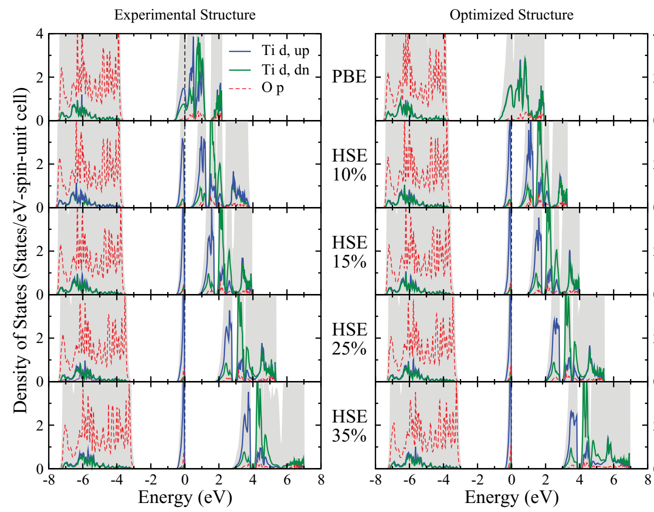

FIG. 6. (Color online) l-projected DOS of AFM-G ordered $LaTiO_3$ with experimental (left) and relaxed (right) structures based on PBE and HSE (HSE-35, HSE-25, HSE-15, HSE-10) functionals. The shadow area indicates the total DOS.

In agreement with previous theoretical findings, we find that local DFT, although it furnishes a very good description of the structural properties, is incapable to reproduce the MH insulating state and wrongly stabilize an AFM-A magnetic ordering. HSE delivers a coherent picture which is, however, α dependent as summarized in Table XII and Fig. 6. Regardless the value of the mixing parameter, HSE predicts an insulating ground state. For $\alpha = 0.10$, HSE conveys a band gap of about 0.1/0.2 eV (depending on whether the experimental or the fully optimized structure is adopted), in excellent agreement with experiment. However, we found that for $\alpha \leqslant 0.10$, HSE finds the AFM-A as the most favorable magnetic ordering (like PBE), in contrast with measurements. In order to stabilize the correct G-type AFM arrangement, a larger value of α is required. But, these larger portions of exact exchange lead to a band gap significantly larger than experiment. The strong influence of the adjustable parameters in beyond-DFT methods such as U in DFT + U and α in HSE on the spin ordering, which can lead to the stabilization of wrong or metastable magnetic arrangements, is well known as recently discussed by Gryaznov *et al.*[173] The "optimum" choice is probably $\alpha = 0.15$ for which HSE delivers an AFM-G insulating solution with a band gap of about 0.7–0.8 eV (depending on the structural details) (see Fig. 7). For larger α, the computed band gap is exceedingly large: 1.8 and 2.8 for $\alpha = 0.25$ (Ref. 109) and 0.35, respectively.

The tendency of beyond-DFT methods to overestimate the band gap of $LaTiO_3$ was already reported in literature, based on SIC [1.7 eV (Ref. 112)] and other HSE (Ref. 109) (1.7 eV using $\alpha = 0.25$, in agreement with our data) studies, and attributed to dynamical effects not included at this level of theory.[170] Furthermore, HSE tends to overestimate the magnetic moment of about 30%, again in analogy with previous beyond-DFT studies.

The MH-type character of the band gap is evident by comparing the PBE and HSE DOS given in Fig. 6: the inclusion of nonlocal exchange split the t_{2g} band near E_F, thus opening a

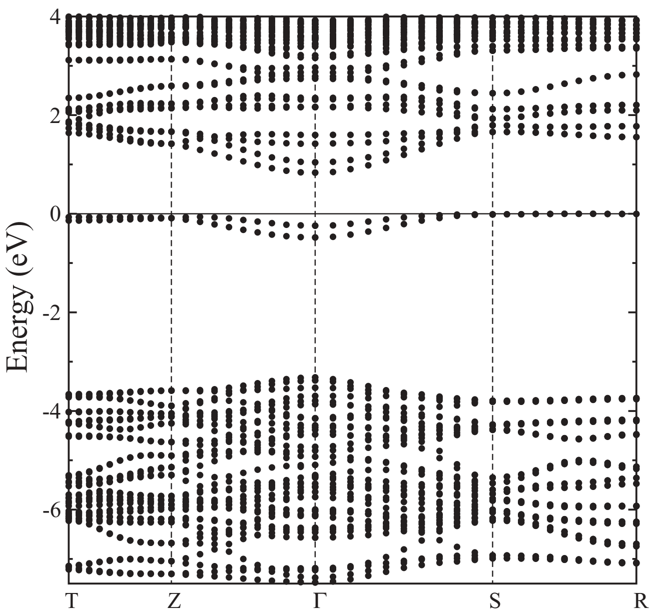

FIG. 7. Band structure of $LaTiO_3$ computed at HSE level ($\alpha = 0.15$) using the optimized structure.

MH band gap between occupied and unoccupied t_{2g} subbands. As expected, the band gap increases with increasing α. The presence of an isolated peak on top of the valence band, well separated from the states beneath, has been also detected by x-ray photoemission spectroscopy (XPS) experiments.[174] The CT gap, defined as the energy separation between the O $2p$ states and the upper t_{2g} Hubbard band is also α dependent, and its value for the optimum 0.15 choice, 4.7 eV, is in excellent agreement with experiment, 4.5 eV.[7]

Finally, we underline that HSE is able to stabilize the correct orbitally ordered state manifested by a chessboard G-type arrangement of differently ordered t_{2g} cigar lobes. We will come back to this point in the next section.

3. d^2: $LaVO_3$

$LaVO_3$ is another challenging material for conventional DFT: it is a $t_{2g}^{\uparrow\uparrow}$ AFM-C Mott insulator, but DFT finds an AFM-C metal. The C-type antiferromagnetic spin ordering is stabilized by the JT-induced bond-length alternations in the *ab* plane which cause the G-type orderings of d_{yz} and d_{zx} orbitals.[60] The experimentally observed MH and CT gaps are 1.1 and 4.0 eV, respectively.[7]

Regardless the fraction of nonlocal exchange, HSE correctly finds a AFM-C MH insulating ground state, in which the gap is open between the lower and the upper MH t_{2g} bands, similarly to $LaTiO_3$ (in PBE the t_{2g} band crosses the Fermi level, see Fig. 8). The best agreement with experiment is achieved for $\alpha = 0.10$–0.15 for which HSE delivers satisfactory values for both the MH ($\approx$0.8–1.4 eV for $\alpha = 0.10$ and 0.15, respectively, as summarized in Table XIII) and CT gaps ($\approx$4.4–4.9 eV for $\alpha = 0.10$ and 0.15, respectively). Similarly to all other theoretical DFT and beyond-DFT approaches, HSE tends to overestimate the magnetic moment. It has been proposed that the origin of this discrepancy could be

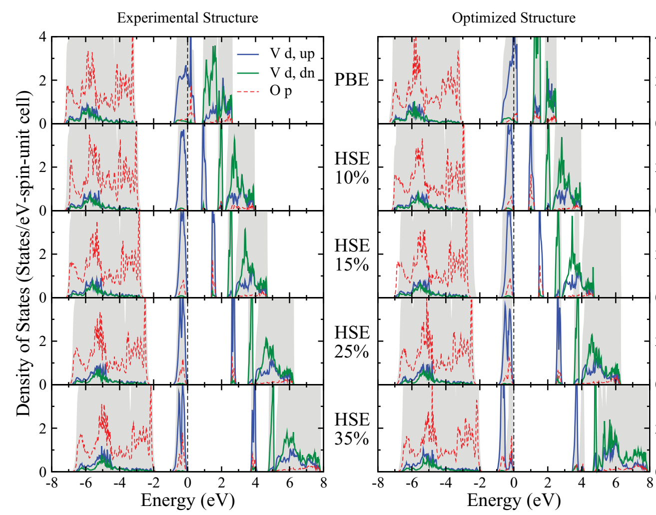

FIG. 8. (Color online) l-projected DOS of AFM-C ordered $LaVO_3$ with experimental (left) and relaxed (right) structures based on PBE and HSE (HSE-35, HSE-25, HSE-15, HSE-10) functionals. The shadow area indicates the total DOS.

an unquenched orbital magnetization or spin-orbit-induced magnetic canting.[55]

The band structure of $LaVO_3$ computed for the representative case $\alpha = 0.15$ is displayed in Fig. 9. Also, this HSE is able to stabilize the correct G-type orbitally ordered state. This will be discussed in more details in the next section.

4. d^3: $LaCrO_3$

Under equilibrium conditions, P_{nma}-distorted $LaCrO_3$ exhibits a G-type AFM insulating ground state with the Cr^{+3} cation in the d^3 electron configuration $t_{2g}^{\uparrow\uparrow\uparrow}$. The optical experiments by Arima *et al.* reported a coexistence of CT and MH-type excitations in $LaCrO_3$ at 3.4 eV.[7] These findings have

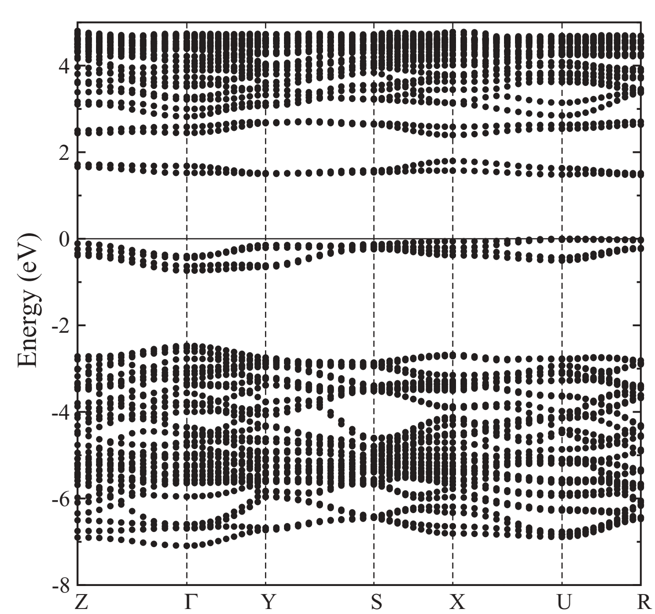

FIG. 9. Band structure of $LaVO_3$ computed at HSE level ($\alpha = 0.15$) using the optimized structure.

TABLE XIII. The band gap Δ (eV), magnetic moment m (μ_B/V), magnetic energy (given with respect to the FM energy, in meV) of $LaVO_3$ calculated by PBE and HSE (HSE-35, HSE-25, HSE-15, HSE-10) using both the experimental and relaxed structures (Table IV). Other theoretical values are also listed for comparison, along with the experimental measurements.

	Theory				
	Optimized structure				
	HSE-35	HSE-25	HSE-15	HSE-10	PBE
Δ	3.42	2.43	1.455	0.885	0.000
m	1.876	1.855	1.819	1.782	1.625
A-AFM	−73	−54	23	43	−77
C-AFM	−124	−114	−144	−177	−216
G-AFM	−96	−98	−30	33	137
	Experimental structure				
	HSE-35	HSE-25	HSE-15	HSE-10	PBE
Δ	3.675	2.535	1.380	0.810	0.000
m	1.882	1.858	1.813	1.774	1.629
A-AFM	−2	33	16	11	−64
C-AFM	−105	−119	−151	−179	−124
G-AFM	−89	−80	−52	−11	203
	Other works				
	LDA	LDA + U	GW	HF	
Δ	0.1[a]	0.7 [b], 0.92[c] 1.2[d]	2.48[c]	3.3[e], 0.9[f]	
m	1.47[a], 1.85[b]	1.98[b], 1.79[c] 1.70[d]	1.79[c]	1.8[e],1.64[f]	
A-AFM	9[a]	3.7[d]			
C-AFM	−35[a]	−38.3[d]			
G-AFM	17[a]	−14.8[d]			
	Experiment				
Δ			1.1[g]		
m			1.3[h]		

[a]Reference 60.
[b]Reference 55.
[c]Reference 78.
[d]Reference 66.
[e]Reference 57.
[f]Reference 72.
[g]Reference 175.
[h]Reference 7.

been explained by several theoretical HF,[57] LDA + U,[59] GW (Ref. 78) studies in terms of a significant mixing between Cr t_{2g} and O p states at the top of the valence band. In particular, the LDA + U study of Yang and co-workers has shown that the CT/MH character of the band gap is strongly U dependent: for small values of U ($U < 5$ eV), the top of the valence band is mainly formed by t_{2g} states and the gap is predominantly MH, but for larger U ($U > 5$ eV), the O p bands are progressively shifted towards higher energy, thus reducing the size of the charge-transfer gap which becomes indistinguishable from the MH one. Our HSE calculations confirm this picture as shown in the DOS plotted in Fig. 10: the O_p-Cr_d mixing at the top of the valence band increases with increasing α. As expected, α also influences the predicted band-gap size which is found to be much smaller than experiment at purely PBE level (1.2 eV) and reaches the value 3.0 eV for $\alpha = 0.15$, in good agreement with the reported optical gap. For larger α, the gap starts to

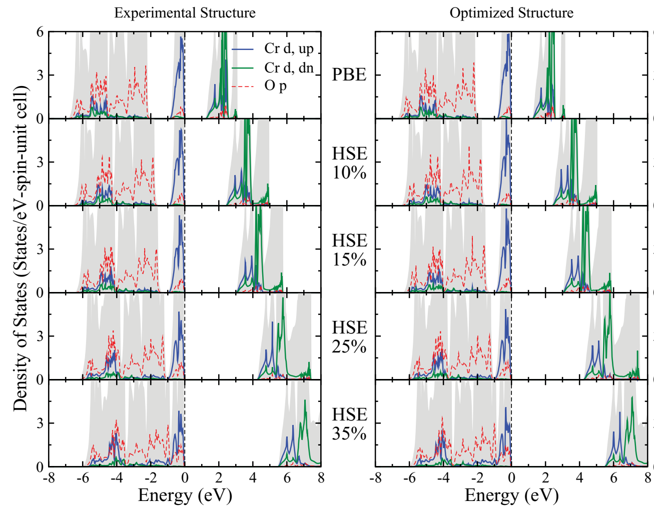

FIG. 10. (Color online) l-projected DOS of AFM-G ordered $LaCrO_3$ with experimental (left) and relaxed (right) structures based on PBE and HSE (HSE-35, HSE-25, HSE-15, HSE-10) functionals. The shadow area indicates the total DOS.

deviate substantially from the measure value, and becomes exceedingly large for $\alpha = 0.35$ (see Table XIV). The band structure corresponding to the optimum $\alpha = 0.15$ choice is displayed in Fig. 11. The G-type spin ordering is very robust at any value of α and the magnetic moment changes by only $0.2\mu_B$ going from $\alpha = 0$ ($\approx 2.6\mu_B$) to $\alpha = 0.35$ ($\approx 2.8\mu_B$). Also, in this case the electronic and magnetic properties obtained from the optimized structure are essentially identical to those corresponding to the experimental structure.

A different interpretation of the band structure and optical properties of $LaCrO_3$ was proposed in 2008 by Ong and co-workers who suggested that $LaCrO_3$ should not be considered a strongly correlated material.[75] These authors have attributed

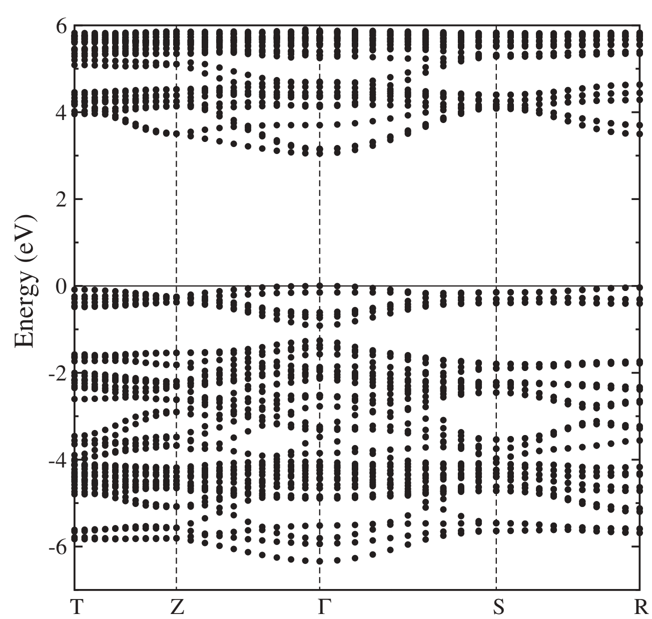

FIG. 11. Band structure of $LaCrO_3$ computed at HSE level ($\alpha = 0.15$) using the optimized structure.

TABLE XIV. The band gap Δ (eV), magnetic moment m (μ_B/Cr), magnetic energy (given with respect to the FM energy, in meV) of $LaCrO_3$ calculated by PBE and HSE (HSE-35, HSE-25, HSE-15, HSE-10) using both the experimental and relaxed structures (Table V). Other theoretical values are also listed for comparison, along with the experimental measurements.

	Theory				
	Optimized structure				
	HSE-35	HSE-25	HSE-15	HSE-10	PBE
Δ	5.475	4.230	3.000	2.415	1.245
m	2.866	2.836	2.790	2.756	2.643
A-AFM	−79	−91	−108	−121	−166
C-AFM	−160	−184	−221	−245	−309
G-AFM	−226	−258	−305	−338	−432
	Experimental structure				
	HSE-35	HSE-25	HSE-15	HSE-10	PBE
Δ	5.460	4.245	3.030	2.430	1.245
m	2.868	2.835	2.784	2.748	2.626
A-AFM	−76	−91	−113	−128	−171
C-AFM	−170	−203	−249	−281	−375
G-AFM	−233	−275	−335	−376	−494
	Other works				
	LDA	LDA + U	GW	HF	
Δ	1.40/3.4[a]	1.04[b], 1.40[a]	3.28[b]	4.5[c]	
m	2.56[a]	2.58[b], 3.00[d]	2.38[b]	3.0[c]	
	Experiment				
Δ	3.4[e]				
m	2.45[f], 2.8[g], 2.49[h]				

[a]Reference 75.
[b]Reference 78.
[c]Reference 57.
[d]Reference 59.
[e]Reference 7.
[f]Reference 176.
[g]Reference 177.
[h]Reference 178.

the 3.4-eV CT gap as the excitation from the top of the wide O p band below the t_{2g} states to the bottom of the Cr d unoccupied band, and called for a new optical experiment to confirm the presence of a smaller MH gap of 2.38 eV open between Cr t_{2g} and Cr e_g bands, which would justify the green-light color of $LaCrO_3$. We are not aware of more recent experimental data in support of this interpretation.

5. d^4: $LaMnO_3$

$LaMnO_3$ is one of the most studied perovskites. Its properties have been widely studied both experimentally and theoretically as mentioned in the Introduction. The initial tentative assignment of Arima and co-workers on the CT electronic nature of $LaMnO_3$ was successively disproved and nowadays it is widely accepted that $LaMnO_3$ represents the prototypical example of a JT-distorted MH orbitally ordered antiferromagnetic (type-A) insulator.[41,179,180] In discussing the structural properties, we have underlined that $LaMnO_3$ is a very critical case for conventional band theory due to the small but crucial JT distortions which are only marginally captured by PBE. The drawbacks of standard DFT are also reflected in the electronic and magnetic properties summarized in Fig. 12 and Table XV, especially for the theoretically relaxed structure. Using the optimized geometry, PBE favors the wrong magnetic ordering (FM) and stabilizes a metallic solution, whereas by adopting the experimental structure, the correct AFM-A insulating ground state is stabilized, but the value of the band gap, 0.23 eV, is significantly smaller than the experimental one, 1.1–2.0 eV (this is in agreement with previous studies[71,83]). This indicates that the JT distortions alone are sufficient to open up a band gap in $LaMnO_3$, but in order to predict a more accurate value, it is necessary to go beyond DFT. In fact, turning to HSE the situation improves significantly and the results achieved within the theoretically optimized geometrical setup are essentially identical to those obtained for the experimental structure. The only significant difference regards the relative stability of the AFM-A ordering with respect to the FM one. For $\alpha = 0.10$, the FM ordering is still more favored over the AFM-A one using the optimized geometry, but by adopting the experimental the AFM-A arrangement becomes the most stable one. For larger values of α, both structural setups lead to essentially the same relative stability among all considered spin arrangements. As expected, the band gap increases linearly with increasing mixing parameter and the best agreement with the measured values is reached again for $\alpha = 0.15$ (≈1.6 eV, well within the experimental range of variation). The band gap is open between occupied and unoccupied Mn e_g states, which are almost completely separated from the other bands, as clarified in the band-structure plot provided in Fig. 13. The associated orbitally ordered state will be presented in the next section. The HSE prediction for the Mn magnetic moment is in good agreement with low-temperature measurements (3.7–3.87μ_B) (Refs. 154 and 186) and previous B3LYP data (∼3.8μ_B).[67,83] We observe a small increase of the magnetic moment with increasing mixing parameter, a general tendency noticed for the other LaMO$_3$ compounds. A more extensive discussion of the ground-state properties of $LaMnO_3$ can be found in our previous works.[41,89]

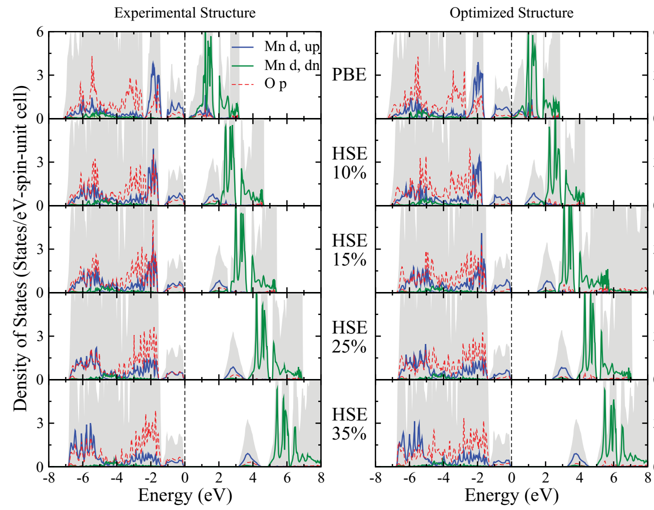

FIG. 12. (Color online) l-projected DOS of AFM-G ordered $LaMnO_3$ with experimental (left) and relaxed (right) structures based on PBE and HSE (HSE-35, HSE-25, HSE-15, HSE-10) functionals. The shadow area indicates the total DOS.

TABLE XV. The band gap Δ (eV), magnetic moment m (μ_B/Mn), magnetic energy (given with respect to the FM energy, in meV) of $LaMnO_3$ calculated by PBE and HSE (HSE-35, HSE-25, HSE-15, HSE-10) using both the experimental and relaxed structures (Table VI). Other theoretical values are also listed for comparison, along with the experimental measurements.

	Theory				
	Optimized structure				
	HSE-35	HSE-25	HSE-15	HSE-10	PBE
Δ	3.41	2.47	1.63	0.75	0.00
m	3.78	3.74	3.67	3.65	3.52
A-AFM	−7	−8	−24	3	171
C-AFM	156	182	198	368	564
G-AFM	161	192	208	428	899
	Experimental structure				
	HSE-35	HSE-25	HSE-15	HSE-10	PBE
Δ	3.30	2.40	1.52	1.10	0.23
m	3.78	3.73	3.67	3.62	3.50
A-AFM	−4	−11	−28	−44	−63
C-AFM	164	182	198	202	209
G-AFM	175	195	212	216	228
	Other works				
	GGA	GGA + U	B3LYP	HF	GW
Δ	0.70[a]	1.18[a]	2.30[b]	3.0[c]	1.6[d], 1.68[e]
m	3.33[a]	3.46[a]	3.80[b]	3.9[c]	3.16[d]
	3.39[f]		3.77[g]	3.96[g]	3.51[e]
	Experiment				
Δ	1.1[h], 1.7[i], 1.9[j], 2.0[k]				
m	3.87[l], 3.7[m], 3.42[n]				

[a]Reference 83.
[b]Reference 64.
[c]Reference 57.
[d]Reference 78.
[e]Reference 41.
[f]Reference 63.
[g]Reference 67.
[h]Reference 7.
[i]Reference 144.
[j]References 181.
[k]Reference 182 and 183.
[l]Reference 184.
[m]Reference 154.
[n]Reference 185.

6. d^5: $LaFeO_3$

The electronic configuration of Fe^{3+} ion in $LaFeO_3$ is the high-spin state $(t_{2g}^{\uparrow\uparrow\uparrow})(e_g^{\uparrow\uparrow})$. Below the rather high magnetic ordering temperature $T_N = 750$ K,[187] $LaFeO_3$ displays a G-type AFM spin ordering, and the d^5 spin saturation prevents the formation of orbital ordering. Arima[7] reported that the spectrum of $LaFeO_3$ is similar to that of $LaMnO_3$, except for an increase of the insulating gap which is found to be 2.1–2.4 eV, about 0.5 eV larger than the $LaMnO_3$ energy gap. The band gap is opened between the predominantly O p and Fe e_g valence band maxima and the lowest unoccupied t_{2g} band as shown in the density of states of Fig. 14. As such, $LaFeO_3$ should be considered an intermediate CT/MH insulator, as originally suggested by Arima, who found almost identical CT and MH gaps.[7] PBE does an appreciable job in predicting the correct AFM-G insulating ground state, although the value of the band gap, ≈0.6 eV, is significantly underestimated with respect to experiment (see the collection of electronic and magnetic data in Table XVI). Similarly, the PBE estimates of the magnetic moment, 3.7 μ_B, are below the observed value. However, it should be noted that the available low-temperature experimental measures of the magnetic moments are very different, 3.9μ_B (Ref. 189) and 4.6μ_B,[176] thus a firm comparison is presently out of reach.

The best agreement with the experimental gap is obtained also in this case for $\alpha = 0.15$ for which HSE gives a gap of about 2.4 eV, for both the optimized and experimental structures (this is not surprising considering that in $LaFeO_3$

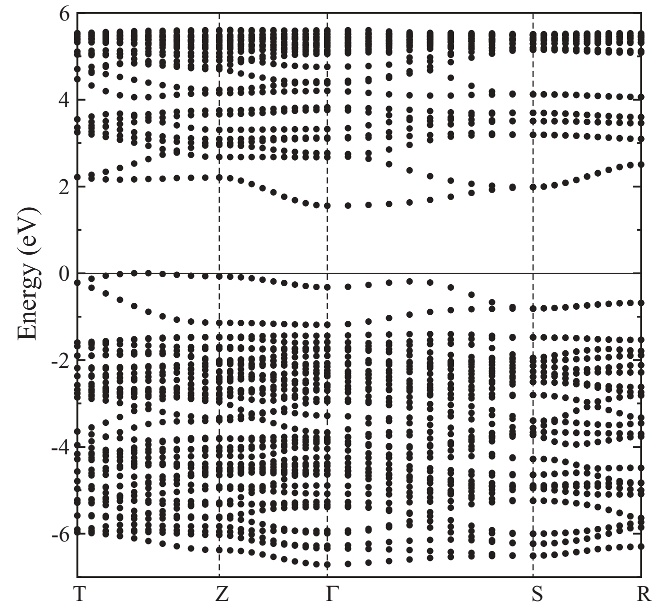

FIG. 13. Band structure of $LaMnO_3$ computed at HSE level ($\alpha = 0.15$) using the optimized structure.

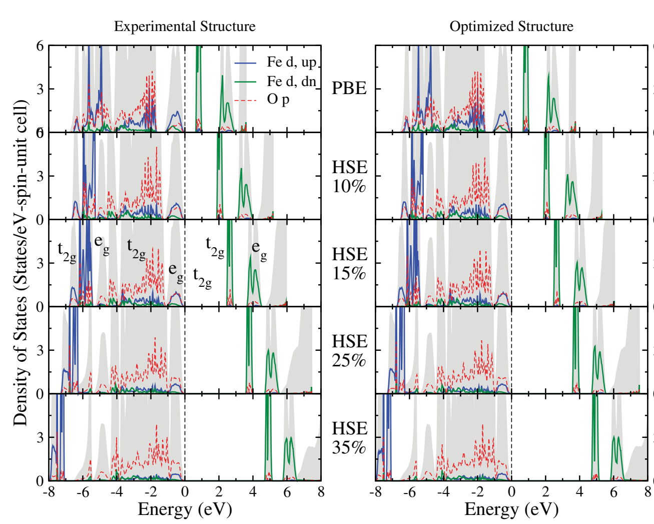

FIG. 14. (Color online) l-projected DOS of AFM-G ordered $LaFeO_3$ with experimental (left) and relaxed (right) structures based on PBE and HSE (HSE-35, HSE-25, HSE-15, HSE-10) functionals. The shadow area indicates the total DOS.

TABLE XVI. The band gap Δ (eV), magnetic moment m (μ_B/Fe), magnetic energy (given with respect to the FM energy, in meV) of $LaFeO_3$, calculated by PBE and HSE (HSE-35, HSE-25, HSE-15, HSE-10) using both the experimental and relaxed structures (Table VII). Other theoretical values are also listed for comparison, along with the experimental measurements.

	Theory				
	Optimized structure				
	HSE-35	HSE-25	HSE-15	HSE-10	PBE
Δ	4.680	3.570	2.460	1.875	0.660
m	4.198	4.110	4.001	3.933	3.719
A-AFM	−259	−323	−417	−487	−75
C-AFM	−530	−653	−832	−947	−278
G-AFM	−760	−930	−1166	−1316	−696
	Experimental structure				
	HSE-35	HSE-25	HSE-15	HSE-10	PBE
Δ	4.665	3.570	2.445	1.875	0.615
m	4.202	4.111	3.998	3.927	3.708
A-AFM	−251	−321	−427	−511	−9
C-AFM	−518	−655	−854	−993	−134
G-AFM	−742	−930	−1194	−1372	−552
	Other works				
	LDA	LDA + U	GW	HF	
Band gap	0.0[a]	0.10[b], 2.1[a]	1.78[b]	4.0[c]	
m	3.5[a]	3.54[b], 4.1[a]	3.37[b]	4.6[c]	
	Experiment				
Δ			2.1[d], 2.4[e]		
m			3.9[f], 4.6[g]		

[a]Reference 59.
[b]Reference 78.
[c]Reference 57.
[d]Reference 7.
[e]Reference 188.
[f]Reference 189.
[g]Reference 176.

the optimized structure differs by less than 1% from the experimental one, as discussed previously). For this value of the mixing parameter, we achieve an excellent comparison with photoemission data of Wadati *et al.*[190] in terms of the position and character of the main peaks at −0.5 eV (Fe e_g, O p), −2 eV (Fe t_{2g}–O p), and −6 eV (Fe e_g, O p). These findings agree with the GW spectra computed by Nohara.[78] By increasing the fraction of HF exchange, the positions of the lowest occupied t_{2g} and e_g states are gradually pushed down in energy and become progressively more localized, whereas the position and bandwidth of the O p band remains essentially unaffected. This leads to a worsening of the comparison with the experiment for $\alpha \geqslant 0.25$. The $\alpha = 0.15$ band structure is shown in Fig. 15. Finally, we note that the energy separation between the unoccupied t_{2g} and e_g states (the two lowest conduction bands, respectively, as indicated in Fig. 14), about 1.3 eV, is almost independent from α and in good agreement with x-ray absorption spectroscopy[190] and the GW (Ref. 78) results.

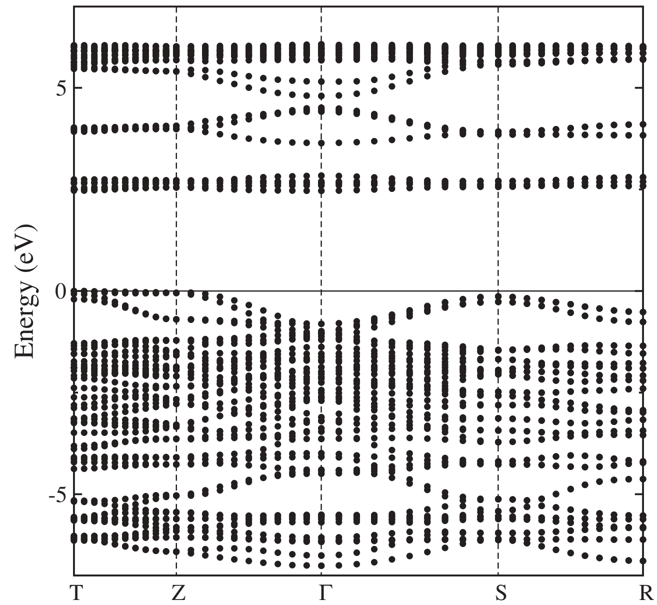

FIG. 15. Band structure of $LaFeO_3$ computed at HSE level ($\alpha = 0.15$) using the optimized structure.

7. d^6: $LaCoO_3$

The complex magnetic behavior of $LaCoO_3$ represents a great challenge for theory. At low temperature, $LaCoO_3$ is a diamagnetic insulator in which the Co^{3+} are aligned in the low-spin (LS) state $(t_{2g}^{\uparrow\downarrow\uparrow\downarrow\uparrow\downarrow})(e_g^0)$, with a total spin $S = 0$. At about 100 K, it undergoes a transition towards a paramagnetic state associated with magnetic excitations involving high-spin $[(t_{2g}^4)(e_g^2),\ S = 2]$ and intermediate-spin $[(t_{2g}^5)(e_g^1),\ S = 1]$ configurations, and at high temperature ($T \approx 500$ K) it shows a second magnetic anomaly associated with an insulator-to-metal transition.[2,191,192] These issues have been widely discussed in literature, but a general consensus is still missing and their detailed understanding remains highly controversial.[81,84]

Standard LDA (or GGA) predicts a metallic and magnetic ground opposite to experiment.[59,68,82] Conversely, DFT + U can reproduce the correct nonmagnetic insulating state, but the results depend critically on the choice of U and the results seem to be strongly dependent on the specific computational schemes adopted. Small values of U (<2 eV) lead to the erroneous DFT-like solution. It has been shown that the correct LS insulating solution can be obtained using rather different U, ranging from $U \approx 3$ eV (Refs. 73 and 80) to $U \approx 8$ (Refs. 58, 77, and 84). Hsu and co-workers[77] have recently performed an optimization of the value of U based on an accurate account of the structural properties, and show that the best agreement with experiment is achieved for a rather large $U \approx 8.2$ eV.[77] A similar value of U has been also found by Laref *et al.* throughout the inverse response matrices.[84] Finally, using the unscreened hybrid functional PBE0 scheme with the standard choice of the mixing parameter (0.25), Gryaznov *et al.* were able to find the correct LS state with a band gap of 2.5 eV.[82] Our HSE results for $\alpha = 0.25$ deliver a LS gap of 2.4 eV, in excellent agreement with these PBE0 results.

In Table XVII, we collect the values of the band gap for the more stable $S = 0$ HSE solution along with available experimental and other theoretical estimations. The best comparison with experiment is achieved for a rather small $\alpha = 0.05$ for which HSE delivers a band gap of about 0.1 eV, in good agreement with optical measurements, 0.1–0.3 eV (Refs. 7,193) (photoemission data of Chainani *et al.*[141] give

TABLE XVII. The band gap Δ (eV) of nonmagnetic $LaCoO_3$ calculated by PBE and HSE (HSE-35, HSE-25, HSE-15, HSE-10) using both the experimental and relaxed structures (Table VIII). Other theoretical values are also listed for comparison, along with the experimental measurements.

	Theory					
	Optimized structure					
	HSE-35	HSE-25	HSE-15	HSE-10	HSE-05	PBE
Δ	3.480	2.415	1.215	0.660	0.165	0.0
	Experimental structure					
	HSE-35	HSE-25	HSE-15	HSE-10	HSE-05	PBE
Δ	3.390	2.445	1.200	0.615	0.105	0.0
	Other works					
	LDA	LDA + U	PBE0	GW	HF	
Δ	1.06[a], 0.0[b]	1.0[c], 2.06[d] 1.8[e]	2.50[b], 3.14[b]	1.28[f]	3.5[g]	
	Experiment					
Δ	0.3[h], 0.1[i]					

[a]Reference 68.
[b]Reference 82.
[c]Reference 80.
[d]Reference 58.
[e]Reference 193.
[f]Reference 78.
[g]Reference 57.
[h]Reference 7.
[i]Reference 84.

a somehow larger gap of about 0.6 eV). We remind that this value of α leads to the most accurate optimized geometry, as discussed in the previous section (see Fig. 22). From the density of states shown in Fig. 16, we evince that the gap is opened between valence band mixed O p and Co d states and empty d-like Co states, in agreement with the DFT + U and PBE0 results mentioned above. The effect of the inclusion of a fraction of HF exchange is the splitting of the occupied t_{2g} manifold and the e_g states (this forms a continuous band

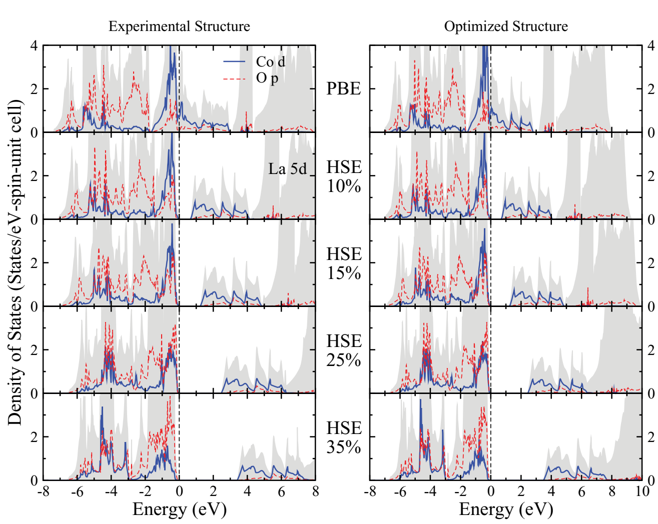

FIG. 16. (Color online) l-projected DOS of nonmagnetic $LaCoO_3$ with experimental (left) and relaxed (right) structures based on PBE and HSE (HSE-35, HSE-25, HSE-15, HSE-10) functionals. The shadow area indicates the total DOS.

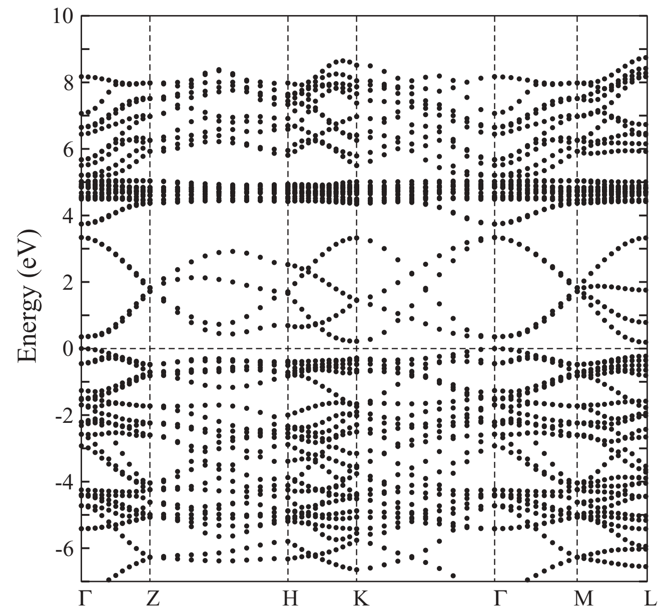

FIG. 17. Band structure of $LaCoO_3$ computed at HSE level ($\alpha = 0.05$) using the optimized structure.

which crosses the Fermi energy at PBE level). The valence band DOS is characterized by three main regions located at −1, −3, and −5 eV, reproducing well the XPS (Ref. 145) and GW (Ref. 78) spectra. Equally satisfactory is the distribution of the conduction band states, with the Co and La d states centered at ≈2 eV and 7–9 eV, respectively.

The band structure plotted in Fig. 17 provides further evidence for the large degree of hybridization of the top of the valence band and the rather dispersive character of the lowest e_g unoccupied states. On the basis of this analysis, $LaCoO_3$ can thus be considered to be predominantly a CT-like (O p → Co d) insulator (in agreement with the initial assignment by Arima[7]), but a Mott mechanism is necessary to split apart the Co d-band crossing E_F at PBE level, possibly indicating minor $t_{2g} \rightarrow e_g$ MH-type excitations, which have not been specifically investigated so far, by both theory and experiment.

8. d^7: $LaNiO_3$

$LaNiO_3$ is a weakly correlated PM metal in which the Ni^{+3} ion possesses the low-spin $3d^7$ configuration $(t_{2g}^{\uparrow\downarrow\uparrow\downarrow\uparrow\downarrow})(e_g^{\uparrow})$. The electron-electron correlation associated with the partially filled Ni $3d^7$ shell is inhibited by an efficient electrostatic screening, originated by the strong Ni $3d$–O $2p$ hybridization (relatively small Ni-O distance), and d-d hybridization (large valence d bandwidth).[7,54,86] The electronic structure of $LaNiO_3$ has been recently extensively investigated and thoughtfully discussed by the group of Rondinelli[86] using an array of several above-standard first-principles methods including LDA + U, PBE0, and HSE.

Our HSE results (summarized in Fig. 18 and Table XVIII) reproduce the trends observed by Rondinelli and co-workers and support their conclusions:

(i) Conventional DFT works fairly well as it provides a correct nonmagnetic metallic solution. This was already pointed out in precedent works.[195,196] We should, however,

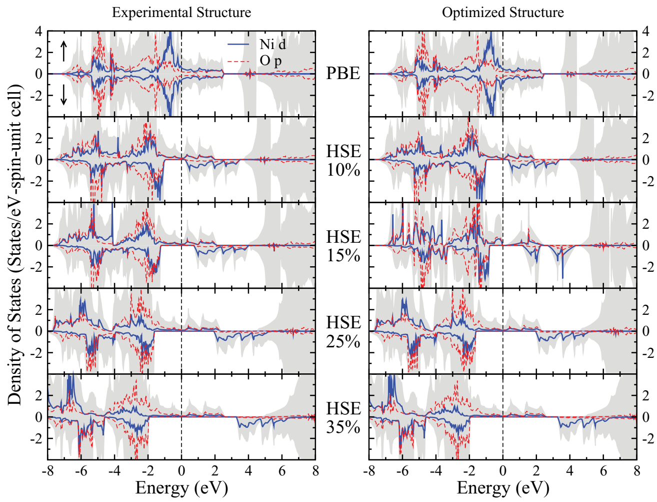

FIG. 18. (Color online) l-projected DOS of FM $LaNiO_3$ with experimental (left) and relaxed (right) structures based on PBE and HSE (HSE-35, HSE-25, HSE-15, HSE-10) functionals. The shadow area indicates the total DOS.

note that for this specific case structural effects are extremely important in the determination of the relative stability between the nonmagnetic ground state and the competing FM solution. Using the experimental structure PBE favors the nonmagnetic case by about 130 meV/f.u., but adopting the PBE-optimized structure, the FM ordering becomes the most stable solution by about 110 meV/f.u.. This should be attributable to the PBE overestimation of the volume (+2.3%), as all other structural properties are described by PBE with an error smaller than 1%

TABLE XVIII. The band gap Δ (eV) and magnetic moment m (μ_B/Ni) of FM ordered $LaNiO_3$, calculated by PBE and HSE (HSE-35, HSE-25, HSE-15, HSE-10) using both the experimental and relaxed structures (Table IX). Other theoretical values are also listed for comparison, along with the experimental measurements.

	Theory				
	Optimized structure				
	HSE-35	HSE-25	HSE-15	HSE-10	PBE
Δ	HM	HM	HM	HM	0.00
m	1.303	1.187	1.034	0.960	0.169
	Experimental structure				
	HSE-35	HSE-25	HSE-15	HSE-10	PBE
Δ	HM	HM	HM	HM	0.0
m	1.308	1.186	1.039	0.956	0.002
	Other works				
	LDA	LDA + U	PBE0/HSE	GW	HF
Δ	0.0[a,b]	0.0[a], HM[b]	HM[b]	0.0[c]	0.3[d]
m	0.0[a,b]	1.1[a], 1.0[b]			
	Experiment				
Δ			0.0[e]		
m			0.0[f] (PM)		

[a]Reference 55.
[b]Reference 86.
[c]Reference 78.
[d]Reference 57.
[e]Reference 7.
[f]Reference 194.

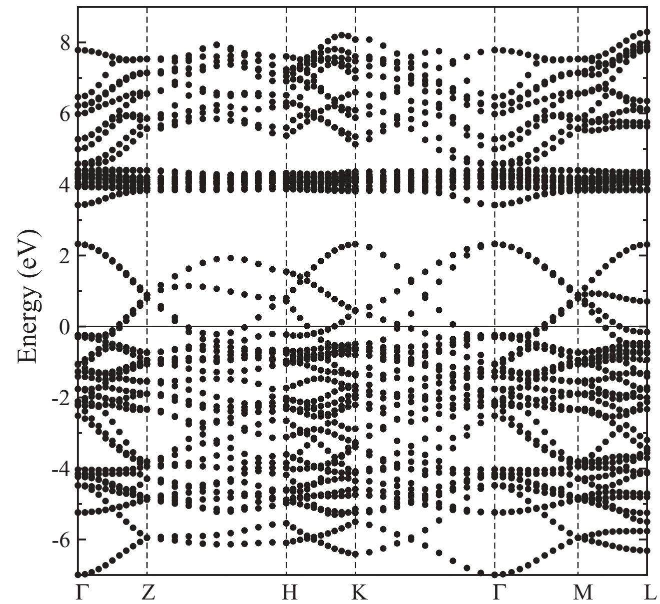

FIG. 19. Band structure of $LaNiO_3$ computed at PBE level using the optimized structure.

(see Table IX). The comparison with PES data gives further support to the quality of the DFT performance, as discussed in Ref. 86. Minor differences have been observed between LSDA and PBE, relative to the width of the valence band, which is better described at LSDA level. The band structure computed at PBE level for the most stable nonmagnetic solution given in Fig. 19 shows evident similarities with the $LaCoO_3$ bands. The major difference is the downward shift of the e_g manifold at the bottom of the conduction band, which now crosses the Fermi level and gets mixed with the lower-lying occupied t_{2g} orbitals. The strong d-p and d-d hybridization is reflected in the highly dispersive character of the valence bands, in accordance with the DOS.

(ii) HSE, similarly to PBE0 and DFT + U,[86] delivers a very lacking picture: $LaNiO_3$ is described as a FM half-metal with a magnetic moment m of about 1 μ_B. m increases gradually as a function of α and reaches the value 1.3 μ_B for $\alpha = 0.35$. The deficient HSE results are mostly due to an excessive downward shift of the t_{2g} manifold (this increases the overall bandwidth with respect to PBE), a strong depletion of Ni d states on top of the valence band, and a much too large exchange splitting. Clearly, the relative strength of these effects increases with increasing α, as clarified in Fig. 18. This makes the comparison with the PES data much worse, in terms of both bandwidth and number and positions of the main peaks.[86] The fundamental failure of hybrid functional for itinerant magnets was already reported by Paier *et al.* for bulk Fe, Co, and Ni.[111]

Although conventional DFT leads to a decent account of the ground state of $LaNiO_3$, it should be emphasized that $LaNiO_3$ is experimentally recognized as being a correlated metal, with important dynamical correlation effects associated with the Ni e_g orbitals[197] which can not be captured at DFT level. More suitable methodologies such as dynamical mean-field theory are needed to appreciate the fundamental nature of $LaNiO_3$, as recently demonstrated.[197–199]

TABLE XIX. The band gap Δ (eV) of nonmagnetic $LaCuO_3$, calculated by PBE and HSE (HSE-35, HSE-25, HSE-15, HSE-10) using both the experimental and relaxed structures (Table X). HSE-35 favors an FM-ordered ground state with $m = 1.197\mu_B$, similarly to the LDA + U calculation of Ref. 53. Other theoretical values are also listed for comparison, along with the experimental measurements.

	Theory				
	Optimized structure				
	HSE-35	HSE-25	HSE-15	HSE-10	PBE
Δ	0.00	0.000	0.000	0.00	0.00
m	0.0	0.000	0.000	0.00	0.00
	Experimental structure				
	HSE-35	HSE-25	HSE-15	HSE-10	PBE
Δ	0.000	0.000	0.000	0.000	0.000
m	0.000	0.000	0.000	0.00	0.00
	Other works				
	LDA	LDA + U	GW	HF	
Δ	0.0[a]	0.0[b], 0.95[a]	0.0[c]	2.2[d]	
m	0.0[a]	0.01[b], 0.98[a]			
	Experiment				
Δ			0.0[e]		
m			0.0[f] (PM)		

[a]Reference 53.
[b]Reference 55.
[c]Reference 78.
[d]Reference 57.
[e]Reference 7.
[f]Reference 161.

9. d^8: $LaCuO_3$

$LaCuO_3$ is a PM metal.[7] Cu^{3+} ions are formally in the low-spin configuration $(t_{2g}^{\uparrow\downarrow\uparrow\downarrow\uparrow\downarrow})(e_g^{\uparrow\downarrow})$ (the t_{2g} shell is fully occupied and the e_g orbitals are half-filled), but it has been argued that this d^8 state is strongly hybridized with the $d^9\underline{L}$ configuration in which $\underline{L}$ denotes a ligand hole, thus suggesting the existence of orbital degeneracy associated with significant Cu-Cu many-body excitations.[200–202] This is another challenging case both for theory (orbital degeneracy and dynamical correlation) and experiment (it is very difficult to to prepare a stoichiometric tetragonal phase of $LaCuO_3$ without oxygen vacancies). Thus, the final methodological comments given for $LaNiO_3$ on the necessity to employ many-body schemes to achieve a fundamentally more accurate theoretical description remain valid for $LaCuO_3$ as well.

Our PBE and HSE results are collected in Table XIX and Figs. 20 and 21. In agreement with the results of Czyżyk and Sawatzky,[53] we find that standard DFT finds the correct metallic nonmagnetic ground state. The DOS (Fig. 20) is characterized by a wide band crossing the Fermi level formed by Cu d (primarily e_g) and O p states, associated with a highly dispersive band (Fig. 21). In analogy with HF (Refs. 57 and 200) and LDA + U (Ref. 53) calculations also within HSE, the G-type AFM insulating state is lower in energy than the nonmagnetic metallic state, in contradiction with experiment. Here, we only report the results for the nonmagnetic solution. From the DOS shown in Fig. 20, we infer that the electronic structure stays almost unchanged with respect to the nonmagnetic PBE case. The only notable

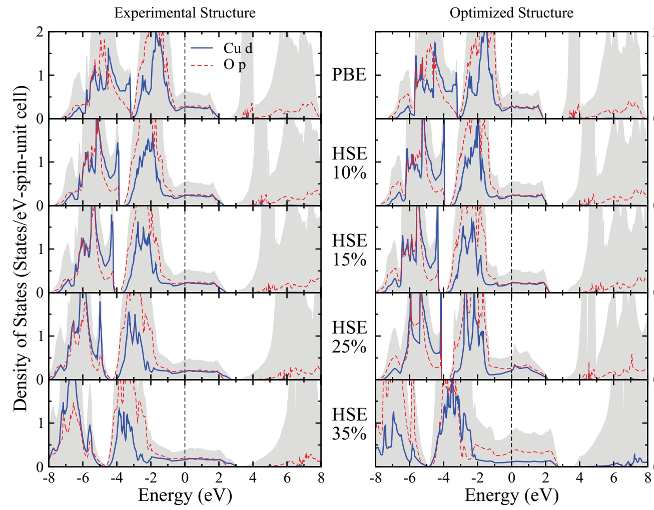

FIG. 20. (Color online) l-projected DOS of nonmagnetic $LaCuO_3$ with experimental (left) and relaxed (right) structures based on PBE and HSE (HSE-25, HSE-15, HSE-10) functionals. The shadow area indicates the total DOS.

difference is a progressive downward shift of the t_{2g} Cu states with increasing α and a gradual further broadening of the Cu d/O p band crossing the E_F.

We conclude this section by providing in Fig. 22 a schematic graphical interpetation of the comparison between computed and measured structural, electronic, and magnetic properties, given in terms of the obtained MARE. A more elaborated discussion will be developed in the next section.

IV. DISCUSSION

From the analysis of the structural, electronic, and magnetic properties developed in the previous section, we have derived a set of optimum values for the mixing parameter ($\alpha_{\rm opt}^{\rm HSE}$) for

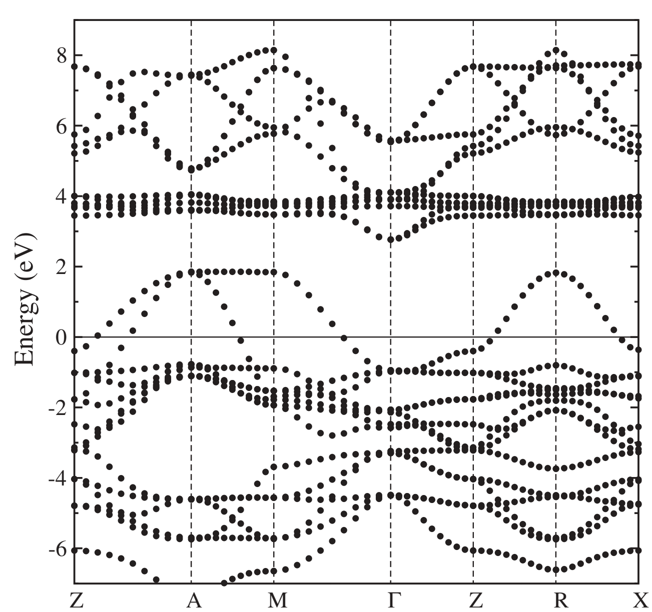

FIG. 21. Band structure of $LaCuO_3$ computed at PBE level using the optimized structure.

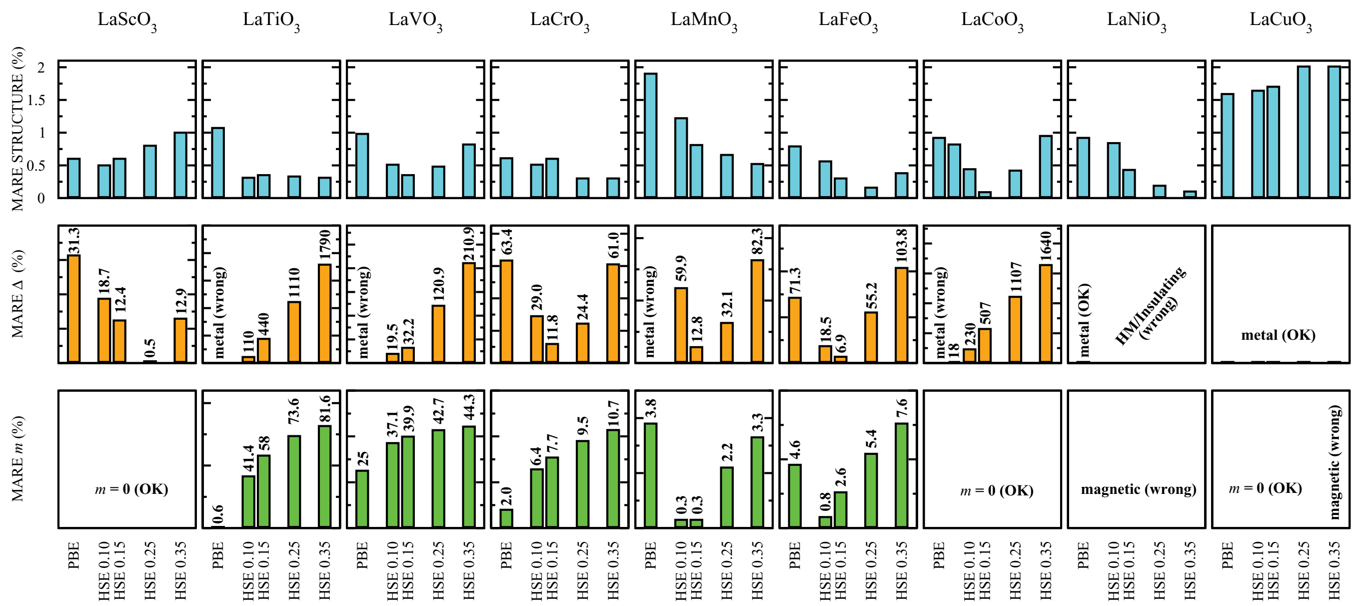

FIG. 22. (Color online) Summary of the MARE for the structural properties (top panel), band gap Δ (middle panel), and magnetic moment m (lower panel), at PBE and HSE levels. For the band gap Δ and the magnetic moment m, the MARE are indicated by the numbers associated to each bar. A few specifications for the labels "OK" and "wrong": (i) $LaScO_3$, m: all methods correctly predict a nonmagnetic ground state; (ii) $LaCoO_3$, m: all methods correctly predict a zero magnetic moment; (iii) $LaNiO_3$, Δ: PBE is the only approach which correctly finds a metallic solution; (iv) $LaNiO_3$, m: all methods wrongly predict a magnetic ground state; (v) $LaCuO_3$, Δ: all methods correctly predict a metallic solution; (vi) $LaCuO_3$, m: PBE and HSE (0.05, 0.15, and 0.25) correctly predict a zero magnetic moment, whereas HSE 0.35 wrongly stabilized a magnetic ground state.

which HSE (and in two cases PBE, i.e., $\alpha = 0$) delivers a substantially correct and quantitatively satisfying description of the LaMO$_3$ series (within the limits discussed previously). This set of $\alpha_{\text{opt}}^{\text{HSE}}$ parameters, collected in Table XX, includes $\alpha = 0.25$ (for the wide-band-gap insulator $LaScO_3$), $\alpha = 0.1$–0.15 (for the MH and intermediate MH/CT insulators $LaTiO_3$-$LaFeO_3$), $\alpha = 0.05$ (for the small-band-gap CT insulator $LaCoO_3$), and $\alpha = 0$ (for metallic $LaNiO_3$ and $LaCuO_3$). As already reported in Sec. III B2, it is important to underline that for $LaTiO_3$ the overall best quantitative agreement with experiment is achieved for $\alpha = 0.1$ (the computed band gap is ≈0.2 eV, almost identical to the measured value), but the incorporation of this fraction of exact exchange in HSE leads to the stabilization of the wrong magnetic ordering, AFM-A instead of AFM-G.

It is instructive at this point to compare the set of parameters $\alpha_{\text{opt}}^{\text{HSE}}$ with the optimum values of α obtained throughout the inverse dielectric constant relation $\alpha_{\text{opt}}^{\epsilon_\infty} \approx \frac{1}{\epsilon_\infty}$ introduced in the computational section [Eq. (7)] and derived by mapping hybrid DFT with GW. The measured dielectric constant ϵ_∞ (Ref. 203) and the corresponding $\frac{1}{\epsilon_\infty}$ values are also listed in Table XX, along with the PEAD HSE values of ϵ_∞ obtained for $\alpha = \alpha_{\text{opt}}^{\text{HSE}}$. Remarkably, the agreement between the measured and calculated ϵ_∞ is very good. The nice correlation between $\alpha_{\text{opt}}^{\text{HSE}}$ and $\alpha_{\text{opt}}^{\epsilon_\infty}$ can be appreciated graphically in Fig. 23. Theses two curves follow a very similar behavior characterized by an initial large value of α for the poorly screened d^0-band insulator $LaScO_3$ followed by a plateau of similar values in the range d^1 ($LaTiO_3$) → d^5 ($LaFeO_3$) and finally a sharp decrease towards the more strongly screened metallic compounds

TABLE XX. Comparison between the set of optimum mixing factors α for the $3d$ perovskite series LaMO$_3$ (M = Sc–Cu) computed throughout the HSE fitting procedure developed in Sec. III and those obtained using the relations $\alpha_{\text{opt}}^{\epsilon_\infty} = 1/\epsilon_\infty$ [Eq. (7), with ϵ_∞ taken from experiment] and $\alpha_{\text{opt}}^{\Delta} = \frac{\Delta^{\text{Expt}} - \Delta^{\text{semilocal}}}{k}$ [Eq. (8)]. The experimental values of the dielectric constant taken from Ref. 203 are compared with the HSE values obtained using the optimum value of α ($\alpha_{\text{opt}}^{\text{HSE}}$).

	$LaScO_3$	$LaTiO_3$	$LaVO_3$	$LaCrO_3$	$LaMnO_3$	$LaFeO_3$	$LaCoO_3$	$LaNiO_3$	$LaCuO_3$
					Optimum α				
$\alpha_{\text{opt}}^{\text{HSE}}$	0.25	0.10 (0.15)	0.10–0.15	0.15	0.15	0.15	0.05	0	0
$\alpha_{\text{opt}}^{\epsilon_\infty}$	0.323	0.125	0.192	0.250	0.204	0.200	0.105	0	0
$\alpha_{\text{opt}}^{\Delta}$	0.245, 0.283	0.050, 0.087	0.115	0.184	0.102, 0.173, 0.190, 0.201	0.117, 0.144	0.029, 0.065	0	0
					Dielectric constant ϵ_∞				
Expt.	3.1	8.0	5.2	4.0	4.9	5.0	9.5	∞	∞
HSE	4.4	8.3	5.9	5.5	5.8	5.7	10.7	∞	∞

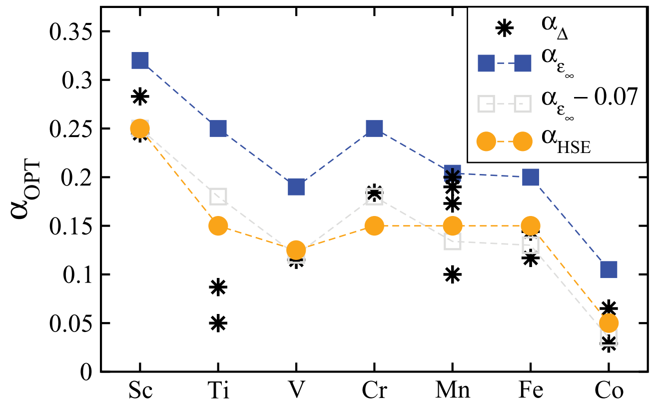

FIG. 23. (Color online) Graphical interpretation of the optimum values of α listed in Table XX showing the correlation between the HSE fitted parameters (HSE fit), the inverse dielectric constant relation ($1/\epsilon_\infty$), and $\alpha^{\Delta}_{\mathrm{opt}}$ [Eq. (8)]. The light-gray squares represent the $1/\epsilon_\infty$ values shifted by 0.07. This shift roughly reflects the amount of screening incorporated in HSE via the screening factor μ as compared to fully unscreened PBE0 (see text).

characterized by a completely filled t_{2g} manifold. For $LaNiO_3$ and $LaCuO_3$, the optimum value of α is zero (not shown). Thus, the α_{opt} curve derived from the HSE fitting procedure conducted by computing a wide set of structural (volume, cell shape, JT distortions, atomic positions) electronic (band gap and DOS), and magnetic (spin ordering, magnetic moment) properties as a function of α reflects well the evolution of the screening properties across the LaMO$_3$ series represented by the dielectric function ϵ_∞.

However, from a quantitative point of view, the two sets of values differ by about 0.07, as clarified graphically by the open squares in Fig. 23. In order to achieve a good quantitative match between the $\alpha^{\mathrm{HSE}}_{\mathrm{opt}}$ and $\alpha^{\epsilon_\infty}_{\mathrm{opt}}$ curves, it is necessary to shift downwards the latter by about 0.07. This behavior is attributable to two main reasons: (i) The relation $\alpha^{\epsilon_\infty}_{\mathrm{opt}} \approx \frac{1}{\epsilon_\infty}$ identifies a proportionality between $\alpha^{\epsilon_\infty}_{\mathrm{opt}}$ and $\frac{1}{\epsilon_\infty}$, not an exact equality (the factor of proportionality is not exactly 1, as discussed in Refs. 133–135). (ii) As already mentioned before, Eq. (7) holds for standard *unscreened* hybrid functionals such as PBE0. HSE is a range-separated screened hybrid functional which contains already a certain degree of screening (controlled by the screening factor μ). Therefore, it is expected that the optimum α derived for PBE0 ($\alpha^{\mathrm{PBE0}}_{\mathrm{opt}}$) will be smaller than the corresponding μ-dependent HSE value ($\alpha^{\mathrm{HSE}}_{\mathrm{opt}}$).[135] Needless to say, in the absence of a systematic study of the role of μ, it is very difficult to quantify its effect on $\alpha^{\mathrm{HSE}}_{\mathrm{opt}}$. We leave this issue open for future studies.

Recently, Alkauskas *et al.* has proposed that an optimal mixing coefficient can generally be found for any material using the formula[135]

$$\alpha^{\Delta}_{\mathrm{opt}} = \frac{\Delta^{\mathrm{Expt}} - \Delta^{\mathrm{semilocal}}}{k}, \tag{8}$$

where Δ^{Expt} and $\Delta^{\mathrm{semilocal}}$ indicate the experimental and semilocal (GGA/LDA) band gap, and $k = d\Delta(\alpha)/d\alpha$ [$\Delta(\alpha)$ represents the variation of the band gap as a function of α].[135] This practical relation takes advantage of the linear relation between Δ and α, which holds true as long as the valence band

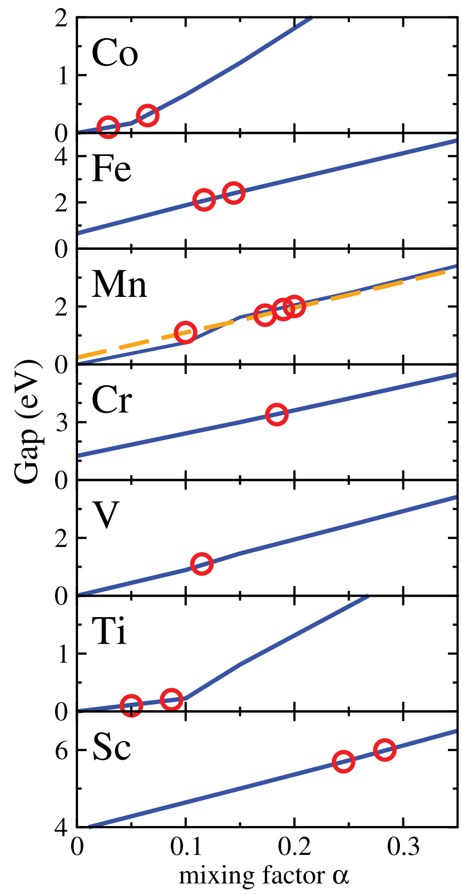

FIG. 24. (Color online) Change of the band gap as a function of α (think lines) and optimum values of α (circles) obtained throughout the practical formula $\alpha^{\Delta}_{\mathrm{opt}} = \frac{\Delta^{\mathrm{Expt}} - \Delta^{\mathrm{semilocal}}}{k}$ [Eq. (8)].

maxima and conduction band minimum (and their associated wave functions) do not change much by changing α.[135] In practice, if the experimental band gap is known, it is sufficient to perform only one hybrid functional calculation for an arbitrary value of α plus one semilocal calculation to derive the optimum value of α. Clearly, this empirical procedure does not guarantee that the so-obtained optimum α is the best choice for what concerns the other ground-state properties. We have already addressed this issue for $LaTiO_3$ for which $\alpha = 0.1$ gives the best band gap but leads to the incorrect magnetic ordering.

The changes of the band gap as a function of α for the series $LaScO_3$-$LaCoO_3$ are reported in Fig. 24. The linearity is well preserved for most of the materials with the exception of the small-band-gap compounds $LaTiO_3$ and $LaCoO_3$ for which a sudden change of $k = d\Delta(\alpha)/d\alpha$ is observed for a critical value of α. A departure from linearity is also found for the JT/MH insulator $LaMnO_3$ if we adopt the fully relaxed structure (full line). This is due to the fact that the cooperative JT distortions, which contribute to the opening of the band gap, do not change linearly with α (as such, the associated wave function will change with α). Indeed, by keeping the atomic coordinates fixed to the experimental positions, the gap grows linearly by increasing α (dashed line).

The values of $\alpha^{\Delta}_{\mathrm{opt}}$ obtained from this set of curves are indicated with empty (red) circles and included in Table XX. For some materials we provide more than one optimum mixing

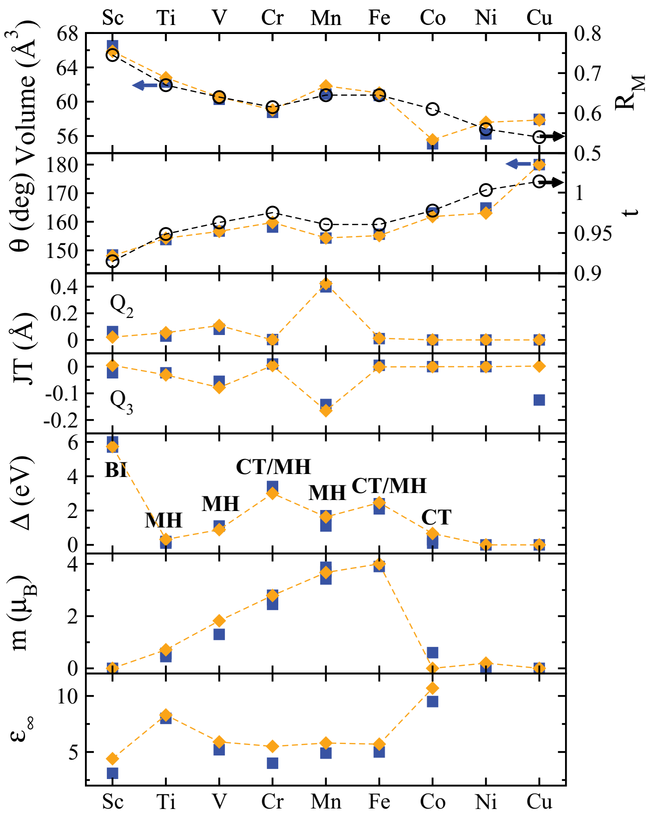

FIG. 25. (Color online) Trend of selected structural (volume V, tilting angle θ, and JT distortions Q_2 and Q_3), electronic (band gap Δ), magnetic (magnetic moment m), and dielectric constant (ϵ_∞) quantities along the LaRO$_3$ series from M = Sc to Cu. We also show the trend of the tolerance factor $t = (R_A + R_O)/\sqrt{2}(R_M + R_O)$, where R_A, R_M, and R_O indicate the ionic radius for La, M = Sc–Cu, and O, respectively, as well as R_M. For $LaTiO_3$ we used $\alpha = 0.1$. The character of the insulating gap is also indicated (BI = band insulator, CT = charge transfer, MH = Mott-Hubbard, CT/MH = mixed CT and MH character).

parameter since different experimental gaps are reported in literature (see previous section). Not surprisingly, we find that the values of $\alpha^{\Delta}_{\rm opt}$ are very similar to the corresponding $\alpha^{\rm HSE}_{\rm opt}$ data, with the exception of $LaTiO_3$ and to a lesser extent $LaMnO_3$, and correlates well with $\alpha^{\epsilon_\infty}_{\rm opt}$, as visualized in Fig. 23.

Now, with the rough-and-ready set of optimum HSE-fitted values $\alpha^{\rm HSE}_{\rm opt}$, we conclude this paper by providing a general picture of the variation of the properties of LaMO$_3$ from M = Sc to Cu by comparing our computed results with the available experimental data. Figure 25 shows the remarkably good agreement between the calculated and measured values of the volume (V), tilting angle (θ), JT distortion, band gap (Δ), magnetic moment (m), and dielectric constant (ϵ_∞). The correlation between V and R_M, as well as between θ and t was already discussed at the beginning of Sec. III A. The variation of the magnetic moment as a function of M can be easily understood in terms of the progressive t_{2g} and e_g band fillings in the high-spin compounds $LaTiO_3$ (${t_{2g}}^{\uparrow}$, $m = 0.51\mu_B$), $LaVO_3$ (${t_{2g}}^{\uparrow\uparrow}$, $m = 1.3\mu_B$), $LaCrO_3$ (${t_{2g}}^{\uparrow\uparrow\uparrow}$, $m = 2.63\mu_B$), $LaMnO_3$ (${t_{2g}}^{\uparrow\uparrow\uparrow}{e_g}^{\uparrow}$, $m = 3.66\mu_B$), and $LaFeO_3$ (${t_{2g}}^{\uparrow\uparrow\uparrow}{e_g}^{\uparrow\uparrow}$, m = 3.9–4.6μB). As already specified, the experimental and computed magnetic moments of $LaCoO_3$ should be taken with a certain caution. $LaNiO_3$ and $LaCuO_3$ show a nonmagnetic behavior at the PBE level only (we have already reported that a small magnetic moment of $0.169\mu_B$ for $LaNiO_3$ is found for the fully relaxed structure).

The variation of the band gaps with the M species shown in Fig. 25 is rather complex and in line with the earlier observation of Arima[7,203]: we observe a general tendency of the MH gap to increase as the TM atomic number increases, whereas the CT gaps follow an opposite behavior. As expected, there is an apparent correlation between the trend of the band gaps and the optimum fraction of exact exchange displayed in Fig. 23, especially $\alpha^{\Delta}_{\rm opt}$. In LDA + U language, this behavior is interpreted as a correlation between the strength of the effective Coulomb interaction U and the band gap (this becomes particularly evident by comparing the Δ curve in Fig. 25 with Fig. 2 in Ref. 55 showing the changes of the effective U with respect to M).

In Fig. 26, we collect the band structures of LaMO$_3$ obtained using the optimum $\alpha^{\rm HSE}_{\rm opt}$ values showing the variation of the electronic dispersion across the whole series. Starting from the d^0-band insulator $LaScO_3$ the addition of one d electron creates a highly localized t_{2g} state right below E_F in $LaTiO_3$. The gradual filling of this t_{2g} manifold leads to a continuous increase of the bandwidth from ${t_{2g}}^1$ ($LaTiO_3$) to ${t_{2g}}^3$ ($LaCrO_3$), connected with a gradual increase of the crystal-field splitting. In $LaMnO_3$, the fully occupied t_{2g} band is pushed down in energy and the valence band maxima are dominated by the half-filled ${e_g}^1$ subbands. The e_g orbital gets completely filled in $LaFeO_3$, which is the last member of the series having a predominantly MH gap. The inclusion of one additional electron yields a sudden change of the band structure manifested by a high increase of p-d hybridization and bandwidth around E_F, which finally leads to the onset of a metallic state in $LaNiO_3$ and $LaCuO_3$.

Three members of the LaMO$_3$ family ($LaTiO_3$, $LaVO_3$, and $LaMnO_3$) are known to display orbital ordering (OO) associated with the partially filled t_{2g} and e_g orbitals located on top of the valence band (these states are demarcated by thick lines in Fig. 26). A visual representation of the OO states derived from the optimum HSE wave functions is shown in Fig. 27 in terms of charge density isosurfaces of the highest occupied d states. In the following, we describe briefly the most important characteristics of the observed OO states.

(i) In $LaTiO_3$, where the OO originates from the single t_{2g} electron, the lobes have a quasi-cigarlike shape with asymmetric contributions along the two main directions, indicating an almost identical occupation of the three xy, xz, and yz t_{2g} shells. Coplanar lobes are arranged in a chessboardlike way with a sign alternation along z, in good agreement with previously reported theoretical[112,170,204] and experimental works.[148,205] There is a clear connection between this chessboardlike Ti d^1 ordering and the JT structural instability, which is manifested by the tendency of the occupied t_{2g} state to lie along the longer Ti-O bond. This also explains why the chessboardlike OO in $LaTiO_3$ is not as much evident as in $LaMnO_3$: in $LaTiO_3$ the difference between the distinct Ti-O bond lengths Ti-O$_s$, Ti-O$_m$, Ti-O$_l$, quantified by the JT parameters Q_2 and Q_3, is about one order of magnitude smaller than in $LaMnO_3$ (see Tables III and VI).

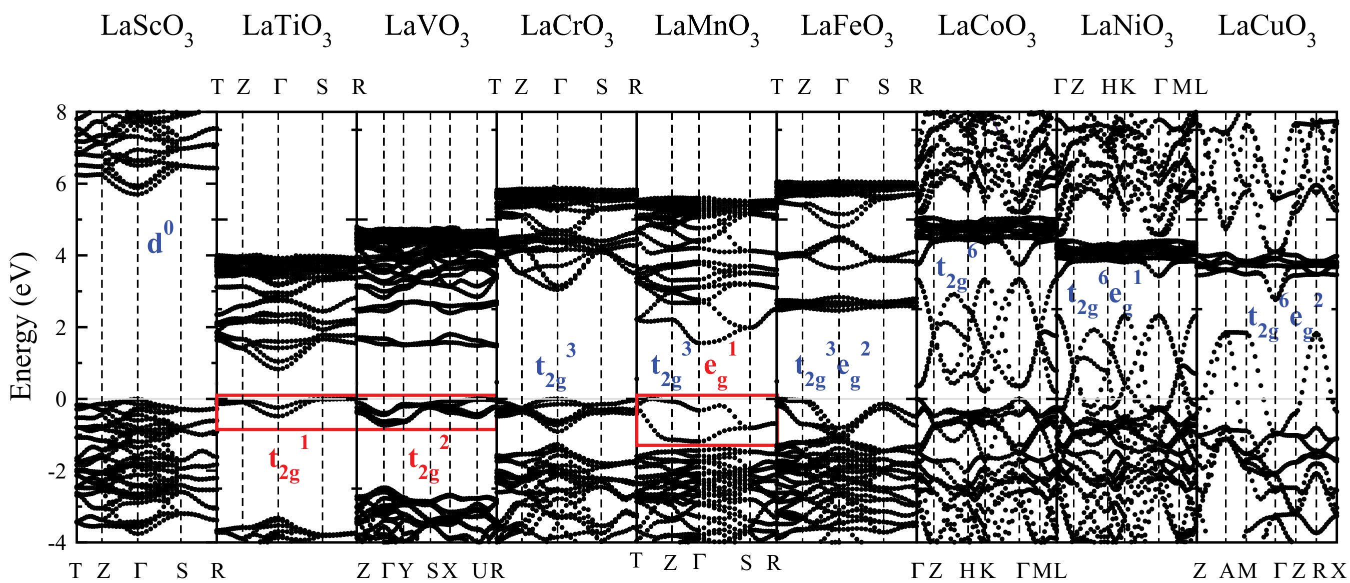

FIG. 26. (Color online) Summary of the HSE electronic dispersion relations showing the complete trend from the band insulator $LaScO_3$ to metallic $LaCuO_3$. The thick (red) lines demarcate the d bands responsible for the observed orbital ordering in $LaTiO_3$ (t_{2g}), $LaVO_3$ (t_{2g}), and $LaMnO_3$ (e_g).

(ii) The V^{3+} ions in $LaVO_3$ can accommodate two electrons in the three possible orbital states d_{xy}, d_{xz}, and d_{yz}. The spins are arranged according to the C-type ordering, whereas the OO state is found to be G-type, in accordance with the Goodenough-Kanamori rules[206] and in agreement with x-ray diffraction[207] and previous GGA (Ref. 60) and HF (Ref. 104) calculations. The distribution of the t_{2g} orbitals in the G-type OO state follows the cooperative JT-induced V-O bond alternation in the xy plane and along the z axis, i.e., the t_{2g} charge density in one specific V site is rotated by 90° with respect to that in the six neighboring V sites (four in-plane and two in the adjacent vertical planes). As already observed for $LaTiO_3$, the t_{2g} orbitals are preferentially occupied along the long-bond direction.

(iii) The C-type OO in $LaMnO_3$, originating from the singly occupied e_g state of the Mn^{3+} $3d$ electrons in the high-spin configuration ${t_{2g}}^3{e_g}^1$, has been extensively studied both experimentally[183,208,209] and theoretically.[179,180] We have also recently addressed this issue throughout a maximally localized Wannier functions representation of the e_g states.[41] This C-type OO state can be written in the form $|\theta\rangle = \cos\frac{\theta}{2}|3z^2 - r^2\rangle + \sin\frac{\theta}{2}|x^2 - y^2\rangle$ with the sign of $\theta \sim 108°$ alternating along x and y and repeating along z, as correctly represented by our HSE charge density plots.

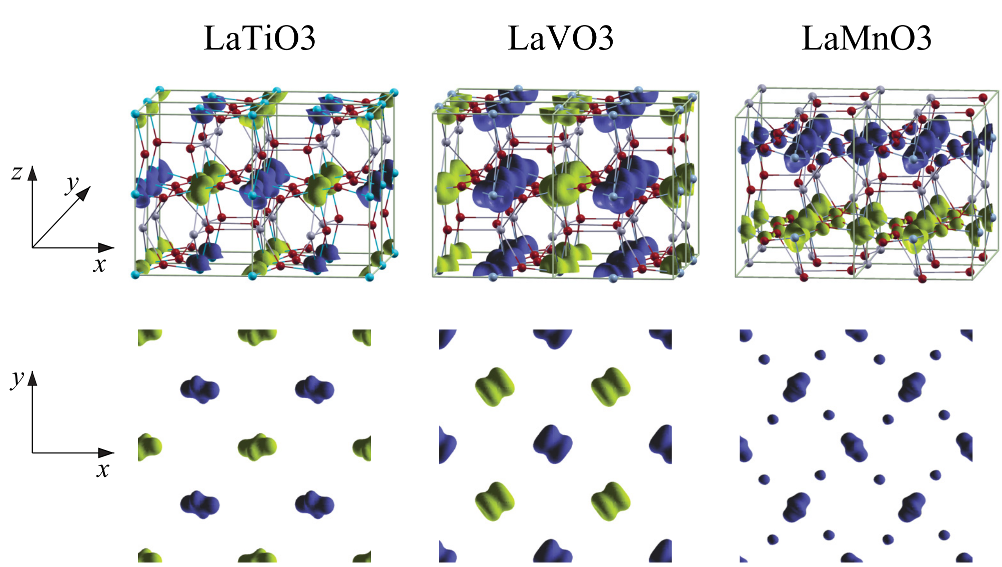

FIG. 27. (Color online) Isosurface of the magnetic orbitally ordered charge density for $LaTiO_3$, $LaVO_3$, and $LaMnO_3$ associated with the topmost occupied bands highlighted in the insets of Fig. 26. Light (yellow) and dark (blue) areas represent spin down and spin up, respectively, indicating the different types of spin orderings in $LaTiO_3$ (G-type), $LaVO_3$ (C-type), and $LaMnO_3$ (A-type). Top panel: three-dimensional view; bottom panel: projection onto the xy plane.

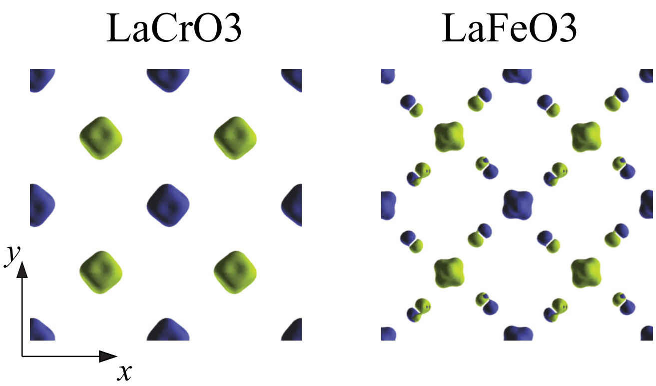

FIG. 28. (Color online) Isosurface of the *non*orbitally ordered magnetic charge density for $LaCrO_3$ (G-type) and $LaFeO_3$ (A-type) associated with the topmost occupied bands (see Fig. 26). Light (yellow) and dark (blue) areas indicate spin down and spin up, respectively.

For comparison, we show in Fig. 28 the similar charge density isosurfaces calculated for $LaCrO_3$ and $LaFeO_3$, in which the half-filling of the t_{2g} and e_g orbitals inhibits any orbital flexibility. As expected, there is no sign of orbital ordering.

We conclude this section with a comparison of the calculated density of valence and conduction states with available x-ray photoemission and x-ray adsorption spectra. This is summarized in Fig. 29. The overall picture is satisfactory in terms of bandwidth, intensity, and peaks position, although some sizable deviations are visible for $LaCrO_3$, $LaFeO_3$, and for the metallic compounds $LaCuO_3$ and $LaNiO_3$. These differences between theory and experiment should be attributable to the approximations included in the adopted computational scheme, as mentioned in the previous section.

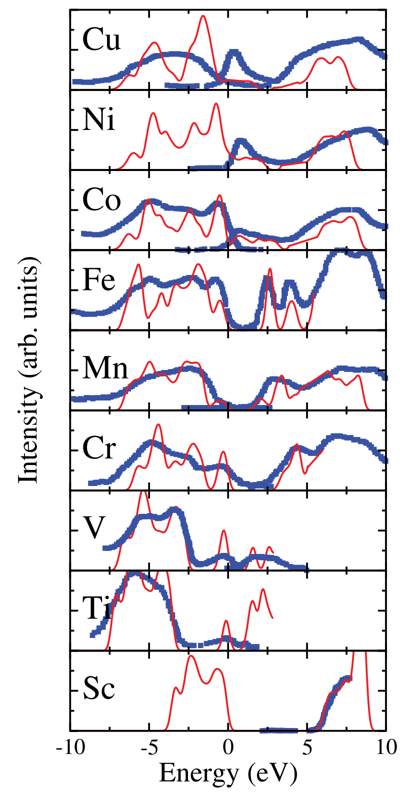

FIG. 29. (Color online) Comparison between experimental (blue squares) and calculated (red full lines) valence and conduction band spectra at the optimum value of the α parameter: (i) $LaScO_3$: $\alpha = 0.25$; (ii) $LaTiO_3$: $\alpha = 0.15$; (iii) $LaVO_3$: $\alpha = 0.15$; (iv) $LaCrO_3$: $\alpha = 0.15$; (v) $LaMnO_3$: $\alpha = 0.15$; (vi) $LaFeO_3$: $\alpha = 0.15$; (vii) $LaCoO_3$: $\alpha = 0.05$; (viii) $LaNiO_3$: $\alpha = 0$; (ix) $LaCuO_3$: $\alpha = 0$. The calculated and measured spectra have been aligned by overlapping the valence band maxima and conduction band minima. The experimental data are taken from the collection of spectra presented in Ref. 78, originally published in separate articles: (i) $LaScO_3$: Ref. 7; (ii) $LaTiO_3$: Ref. 210; (iii) $LaVO_3$: Ref. 211; (iv) $LaCrO_3$: Ref. 212; (v) $LaMnO_3$: Ref. 144; (vi) $LaFeO_3$: Ref. 190; (vii) $LaCoO_3$: Ref. 145; (viii) $LaNiO_3$: Ref. 213; and (ix) $LaCuO_3$: Ref. 200.

V. SUMMARY AND CONCLUSIONS

In summary, we have studied the ground-state properties of the perovskite series $LaMO_3$ by means of screened hybrid DFT following the HSE formulation, based on the inclusion of a fraction of exact HF exchange in the short-range Coulomb kernel of the underlying semilocal PBE exchange-correlation functional. In particular, we have investigated the role of the HSE mixing parameter α on the (i) structural parameters (volume, JT/GFO distortions, lattice parameters, and unit-cell symmetry), (ii) electronic character (band gap, DOS, and band structure), and (iii) spin orderings and magnetic moment, as a function of the gradual filling of the d manifold from $LaScO_3$ (d^0) to $LaCuO_3$ (d^8: $t_{2g}{}^6 e_g{}^2$).

On the basis of a computational fitting of the most relevant experimentally available data, we have derived a set of mixing factors which leads to an accurate qualitative and quantitative description of the physical behavior of all members of the representative $LaMO_3$ family. It is found that, apart from $LaScO_3$, the "optimum" values of α (α_{opt}^{HSE}) are significantly smaller than the routinely used standard choice $\alpha = 0.25$, especially for the end members ($LaScO_3$: $\alpha_{opt}^{HSE} = 0.25$; $LaTiO_3$ and $LaVO_3$: $\alpha_{opt}^{HSE} = 0.10$–$0.15$; $LaCrO_3$, $LaMnO_3$, and $LaFeO_3$: $\alpha_{opt}^{HSE} = 0.15$; $LaCoO_3$: $\alpha_{opt}^{HSE} = 0.05$; $LaNiO_3$ and $LaCuO_3$: $\alpha_{opt}^{HSE} = 0.0$, i.e., for these two cases, PBE is better than HSE). This can be understood by correlating the changes of α_{opt}^{HSE} from Sc to Cu with the corresponding values of the inverse dielectric constant $1/\epsilon_\infty$, and by considering that a certain degree of screening is already included by construction in the HSE functional throughout the screening length μ, at variance with the unscreened parent hybrid functional PBE0 (for which $\mu = 0$). This suggests that the optimum value of α in HSE should be smaller than the corresponding PBE0 one: in our specific case, it is proposed that the difference between α_{opt}^{HSE} and α_{opt}^{PBE0} should be about 0.05–0.07, but a more detailed analysis on the influence of μ is required to achieve more accurate and comprehensive conclusions.

An alternative way to obtain a set of optimum α is the fitting of the band gap only, by applying the practical recipe represented by Eq. (8). However, although this procedure has the clear advantage of reducing considerably the computational cost, it can lead to an erroneous description of other properties (for example, the best-band gap α in $LaTiO_3$ stabilizes the wrong spin ordering) and can only be applied under the assumption that the wave function does not change with α.

For what concerns the description of the modulation of the electronic and magnetic properties across the LaMO_3 series, we found that for all insulating compounds (M = Sc to Co), HSE is capable to capture the localization of the t_{eg}/e_g orbitals and to provide a consistent and quantitatively satisfactory description of all considered quantities, thereby improving the deficient DFT-based predictions.

For the structural properties, on the other hand, PBE performs rather well, delivering optimized geometry within 1%. The only exceptions are the JT parameters in $LaMnO_3$, which PBE finds 60% smaller than experiment. HSE cures this limitation, reproducing quite well the critical JT and GFO structural instabilities, and, in a general, its application improves even further the overall agreement with experiment as compared to PBE.

The complex nature of the PM correlated metals $LaNiO_3$ and $LaCuO_3$, end members of the LaMO_3 series, is only marginally accounted for by PBE and rather poorly treated at the HSE level. This is mostly due to underlying dynamical correlation effects which can not be easily treated at DFT/HF level. For these compounds, PBE might be considered to be a good starting point for more elaborated many-body approaches.

ACKNOWLEDGMENTS

This research was sponsored by the FP7 European Community grant ATHENA. All calculations have been performed on the Vienna Scientific Cluster (VSC).

[1] N. F. Mott, *Metal-Insulator Transitions* (Taylor & Francis, London, 1990).
[2] M. Imada, A. Fujimori, and Y. Tokura, Rev. Mod. Phys. **70**, 1039 (1998).
[3] J. G. Bednorz and K. A. Müller, Z. Phys. B: Condens. Matter **64**, 189 (1986).
[4] R. von Helmolt, J. Wecker, B. Holzapfel, L. Schultz, and K. Samwer, Phys. Rev. Lett. **71**, 2331 (1993).
[5] M. B. Salamon and M. Jaime, Rev. Mod. Phys. **73**, 583 (2001).
[6] K. F. Wang, J. M. Liu, and Z. F. Ren, Adv. Phys. **58**, 321 (2009).
[7] T. Arima, Y. Tokura, and J. B. Torrance, Phys. Rev. B **48**, 17006 (1993).
[8] H. Tanaka and M. Misono, Curr. Opin. Solid State Matter. Sci. **5**, 381 (2001).
[9] J. Suntivich, H. A. Gasteiger, N. Yabuuchi, H. Nakanishi, J. B. Goodenough, and Y. Shao-Horn, Nat. Chem. **3**, 546 (2011).
[10] P. Zubko, S. Gariglio, M. Gabay, P. Ghosez, and J.-M. Triscone, Annu. Rev. Condens. Matter Phys. **2**, 141 (2011).
[11] A. P. Ramirez, J. Phys.: Condens. Matter **9**, 8171 (1997).
[12] J. M. D. Coey, M. Viret, and S. von Molnár, Adv. Phys. **48**, 167 (1999).
[13] I. Loa, P. Adler, A. Grzechnik, K. Syassen, U. Schwarz, M. Hanfland, G. Kh. Rozenberg, P. Gorodetsky, and M. P. Pasternak, Phys. Rev. Lett. **87**, 125501 (2001).
[14] J.-S. Zhou, J. A. Alonso, A. Muoñz, M. T. Fernández-Díaz, and J. B. Goodenough, Phys. Rev. Lett. **106**, 057201 (2011).
[15] A. Asamitsu, Y. Moritomo, Y. Tomioka, T. Arima, and Y. Tokura, Nature (London) **373**, 407 (1995).
[16] C. M. Varma, Phys. Rev. B **54**, 7328 (1996).
[17] R. Ramesh and D. G. Sclom, MRS Bull. **33**, 1006 (2008).
[18] J. Chakhalian, A. J. Millis, and J. Rondinelli, Nat. Mater. **11**, 92 (2012).
[19] A. Kudo and Y. Miseki, Chem. Soc. Rev. **38**, 253 (2009).
[20] S. B. Adler, Chem. Rev. **104**, 4791 (2004).
[21] P. W. Anderson, Phys. Rev. **124**, 41 (1961).
[22] O. Gunnarsson and K. Schönhammer, Phys. Rev. Lett. **50**, 604 (1983).
[23] W. Kohn, Rev. Mod. Phys. **71**, 1253 (1999).
[24] W. Kohn and L. J. Sham, Phys. Rev. **140**, A1133 (1965).
[25] W. Metzner and D. Vollhardt, Phys. Rev. Lett. **62**, 324 (1989).
[26] A. Georges, G. Kotliar, W. Krauth, and M. J. Rozenberg, Rev. Mod. Phys. **68**, 13 (1996).
[27] G. Kotliar, S. Y. Savrasov, K. Haule, V. S. Oudovenko, O. Parcollet, and C. A. Marianetti, Rev. Mod. Phys. **78**, 865 (2006).
[28] I. V. Solovyev, J. Phys.: Condens. Matter **20**, 293201 (2008).
[29] M. Imada and T. Miyake, J. Phys. Soc. Jpn. **79**, 112001 (2010).
[30] P. W. Anderson, Phys. Rev. **115**, 2 (1959).
[31] J. Hubbard, Proc. R. Soc. London, Ser. A **276**, 238 (1963); **277**, 237 (1964); **281**, 401 (1964).
[32] J. Kanamori, Prog. Theor. Phys. **30**, 275 (1963).
[33] C. J. Calzado, J. Cabrero, J. P. Malrieu, and R. Caballol, J. Chem. Phys. **106**, 2728 (2002); **106**, 3985 (2002).
[34] I. D. Prodan, Gustavo E. Scuseria, and Richard L. Martin, Phys. Rev. B **76**, 033101 (2007).
[35] I. D. R. Moreira, C. J. Calzado, J. P. Malrieu, and F. Illas, New J. Phys. **9**, 369 (2007).
[36] V. Bayer, C. Franchini, and R. Podloucky, Phys. Rev. B **75**, 035404 (2007).
[37] G. Fischer, M. Däne, A. Ernst, P. Bruno, M. Lüeders, Z. Szotek, W. Temmerman, and W. Hergert, Phys. Rev. B **80**, 014408 (2009).
[38] C. Boilleau, N. Suaud, R. Bastardis, N. Guihéry, and J.-P. Malrieu, Theor. Chem. Acc. **126**, 231 (2010).
[39] R. Kováčik and C. Ederer, Phys. Rev. B **81**, 245108 (2010).
[40] R. Kováčik and C. Ederer, Phys. Rev. B **84**, 075118 (2011).
[41] C. Franchini, R. Kováčik, M. Marsman, S. Sathyanarayana Murthy, J. He, C. Ederer, and G. Kresse, J. Phys.: Condens. Matter **24**, 235602 (2012).
[42] J. P. Perdew, A. Ruzsinszky, J. Tao, V. N. Staroverov, G. E. Scuseria, and G. I. Csonka, J. Chem. Phys. **123**, 062201 (2005).
[43] R. G. Parr and W. Yang,*Density-Functional Theory of Atoms and Molecules* (Oxford University Press, Oxford, UK, 1989).
[44] V. I. Anisimov, J. Zaanen, and O. K. Andersen, Phys. Rev. B **44**, 943 (1991).
[45] J. P. Perdew and A. Zunger, Phys. Rev. B **23**, 5048 (1981).
[46] A. Svane and O. Gunnarsson, Phys. Rev. Lett. **65**, 1148 (1990).
[47] Z. Szotek, W. M. Temmerman, and H. Winter, Phys. B (Amsterdam) **172**, 19 (1991).
[48] A. Filippetti and N. A. Spaldin, Phys. Rev. B **67**, 125109 (2003).

[49] A. D. Becke, J. Chem. Phys. **98**, 1372 (1993).
[50] L. Hedin, Phys. Rev. **139**, A796 (1965).
[51] C. J. Cramer and D. G. Truhlar, Phys. Chem. Chem. Phys. **11**, 10757 (2009).
[52] J. Heyd, G. E. Scuseria, and M. Ernzerhof, J. Chem. Phys. **118**, 8207 (2003); **124**, 219906 (2006).
[53] M. T. Czyżyk and G. A. Sawatzky, Phys. Rev. B **49**, 14211 (1994).
[54] D. D. Sarma, N. Shanthi, S. R. Barman, N. Hamada, H. Sawada, and K. Terakura, Phys. Rev. Lett. **75**, 1126 (1995).
[55] I. Solovyev, N. Hamada, and K. Terakura, Phys. Rev. B **53**, 7158 (1996).
[56] I. Solovyev, N. Hamada, and K. Terakura, Phys. Rev. Lett. **76**, 4825 (1996).
[57] T. Mizokawa and A. Fujimori, Phys. Rev. B **54**, 5368 (1996).
[58] M. A. Korotin, S. Yu. Ezhov, I. V. Solovyev, V. I. Anisimov, D. I. Khomskii, and G. A. Sawatzky, Phys. Rev. B **54**, 5309 (1996).
[59] Z. Yang, Z. Huang, L. Ye, and X. Xie, Phys. Rev. B **60**, 15674 (1999).
[60] H. Sawada, N. Hamada, K. Terakura, and T. Asada, Phys. Rev. B **53**, 12742 (1996).
[61] H. Sawada, Y. Morikawa, K. Terakura, and N. Hamada, Phys. Rev. B **56**, 12154 (1997).
[62] N. Hamada, H. Sawada, I. Solovyev, and K. Terakura, Phys. B (Amsterdam) **237**, 11 (1997).
[63] P. Ravindran, A. Kjekshus, H. Fjellvåg, A. Delin, and O. Eriksson, Phys. Rev. B **65**, 064445 (2002).
[64] D. Muñoz, N. M. Harrison, and F. Illas, Phys. Rev. B **69**, 085115 (2004).
[65] P. Ravindran, R. Vidya, H. Fjellvåg, and A. Kjekshus, J. Cryst. Growth **268**, 554 (2004).
[66] Z. Fang and N. Nagaosa, Phys. Rev. Lett. **93**, 176404 (2004).
[67] R. A. Evarestov, E. A. Kotomin, Yu. A. Mastrikov, D. Gryaznov, E. Heifets, and J. Maier, Phys. Rev. B **72**, 214411 (2005).
[68] M. Sahnoun, C. Daul, O. Haas, and A. Wokaun, J. Phys.: Condens. Matter **17**, 7995 (2005).
[69] S. Okatov, A. Poteryaev, and A. Lichtenstein, Europhys. Lett. **70**, 499 (2005).
[70] G. Trimarchi and N. Binggeli, Phys. Rev. B **71**, 035101 (2005).
[71] E. A. Kotomin, R. A. Evarestov, Yu. A. Mastrikova, and J. Maier, Phys. Chem. Chem. Phys. **7**, 2346 (2005).
[72] I. V. Solovyev, Phys. Rev. B **74**, 054412 (2006).
[73] K. Knížek, Z. Jirák, J. Hejtmánek, and P. Novák, J. Phys.: Condens. Matter **18**, 3285 (2006).
[74] Hyo-Shin Ahn, Do Duc Cuong, Jaichan Lee, and Seungwu Han, J. Korean Phys. Soc. **49**, 1536 (2006).
[75] K. P. Ong, P. Blaha, and P. Wu, Phys. Rev. B **77**, 073102 (2008).
[76] Y. Nohara, A. Yamasaki, S. Kobayashi, and T. Fujiwara, Phys. Rev. B **74**, 064417 (2006).
[77] H. Hsu, K. Umemoto, M. Cococcioni, and R. Wentzcovitch, Phys. Rev. B **79**, 125124 (2009).
[78] Y. Nohara, S. Yamamoto, and T. Fujiwara, Phys. Rev. B **79**, 195110 (2009).
[79] J. W. Zwanziger, Phys. Rev. B **79**, 033112 (2009).
[80] K. Knížek, Z. Jirák, J. Hejtmánek, P. Novák, and W. Ku, Phys. Rev. B **79**, 014430 (2009).
[81] H. Hsu, P. Blaha, R. M. Wentzcovitch, and C. Leighton, Phys. Rev. B **82**, 100406(R) (2010).
[82] D. Gryaznov, R. A. Evarestov, and J. Maier, Phys. Rev. B **82**, 224301 (2010).
[83] T. Hashimoto, S. Ishibashi, and K. Terakura, Phys. Rev. B **82**, 045124 (2010).
[84] A. Laref and S. J. Lou, J. Phys. Soc. Jpn. **79**, 064702 (2010).
[85] C. Ederer, T. Harris, and R. Kováčik, Phys. Rev. B **83**, 054110 (2011).
[86] G. Gou, I. Grinberg, A. M. Rappe, and J. M. Rondinelli, Phys. Rev. B **84**, 144101 (2011).
[87] E. A. Ahmad, L. Liborio, D. Kramer, G. Mallia, A. R. Kucernak, and N. M. Harrison, Phys. Rev. B **84**, 085137 (2011).
[88] J. Hong, A. Stroppa, J. Íñiguez, S. Picozzi, and D. Vanderbilt, Phys. Rev. B **85**, 054417 (2012).
[89] Jiangang He, Ming-Xing Chen, Xing-Qiu Chen, and Cesare Franchini, Phys. Rev. B **85**, 195135 (2012).
[90] K. Momma and F. Izumi, J. Appl. Crystallogr. **41**, 653 (2008).
[91] W. Y. Hu, M. C. Qian, Q. Q. Zheng, H. Q. Lin, and H. K. Wong, Phys. Rev. B **61**, 1223 (2000).
[92] E. R. Ylvisaker, W. E. Pickett, and K. Koepernik, Phys. Rev. B **79**, 035103 (2009).
[93] J. P. Perdew, K. Burke, and M. Ernzerhof, Phys. Rev. Lett. **77**, 3865 (1996).
[94] Y. S. Su, T. A. Kaplan, S. D. Mahanti, and J. F. Harrison, Phys. Rev. B **61**, 1324 (2000).
[95] M. Mochizuki and M. Imada, New J. Phys. **6**, 154 (2004).
[96] E. Pavarini, A. Yamasaki, J. Nuss, and O. K. Andersen, New J. Phys. **7**, 188 (2005).
[97] X. F. Hao, A. Stroppa, S. Picozzi, A. Filippetti, and C. Franchini, Phys. Rev. B **86**, 014116 (2012).
[98] P. Rivero, I. de P. R. Moreira, G. E. Scuseria, and F. Illas, Phys. Rev. B **79**, 245129 (2009).
[99] P. Rivero, I. de P. R. Moreira, and F. Illas, Phys. Rev. B **81**, 205123 (2010).
[100] O. Gunnarsson, O. K. Andersen, O. Jepsen, and J. Zaanen, Phys. Rev. B **39**, 1708 (1989).
[101] V. I. Anisimov and O. Gunnarsson, Phys. Rev. B **43**, 7570 (1991).
[102] F. Aryasetiawan, M. Imada, A. Georges, G. Kotliar, S. Biermann, and A. I. Lichtenstein, Phys. Rev. B **70**, 195104 (2004).
[103] M. Cococcioni and S. de Gironcoli, Phys. Rev. B **71**, 035105 (2005).
[104] I. V. Solovyev, Phys. Rev. B **73**, 155117 (2006).
[105] K. Karlsson, F. Aryasetiawan, and O. Jepsen, Phys. Rev. B **81**, 245113 (2010).
[106] M. A. L. Marques, J. Vidal, M. J. T. Oliveira, L. Reining, and S. Botti, Phys. Rev. B **83**, 035119 (2011).
[107] J. Paier, R. Hirschl, M. Marsman, and G. Kresse, J. Chem. Phys. **122**, 234102 (2005).
[108] T. Archer, C. D. Pemmaraju, S. Sanvito, C. Franchini, J. He, A. Filippetti, P. Delugas, D. Puggioni, V. Fiorentini, R. Tiwari, and P. Majumdar, Phys. Rev. B **84**, 115114 (2011).
[109] F. Iori, M. Gatti, and A. Rubio, Phys. Rev. B **85**, 115129 (2012).
[110] J. P. Perdew, M. Ernzerhof, and K. Burke, J. Chem. Phys. **105**, 9982 (1996).
[111] J. Paier, M. Marsman, K. Hummer, G. Kresse, I. C. Gerber, and J. G. Ańgyań, J. Chem. Phys. **124**, 154709 (2006).
[112] A. Filippetti, C. D. Pemmaraju, S. Sanvito, P. Delugas, D. Puggioni, and V. Fiorentini, Phys. Rev. B **84**, 195127 (2011).
[113] H. Zenia, G. A. Gehring, and W. M. Temmerman, New J. Phys. **7**, 257 (2005).
[114] A. Filippetti and V. Fiorentini, Eur. Phys. J. B **71**, 139 (2009).
[115] M. Shishkin, M. Marsman, and G. Kresse, Phys. Rev. Lett. **99**, 246403 (2007).

[116]C. Franchini, A. Sanna, M. Marsman, and G. Kresse, Phys. Rev. B **81**, 085213 (2010).
[117]G. Kresse and J. Hafner, Phys. Rev. B **48**, 13115 (1993).
[118]G. Kresse and J. Furthmüller, Comput. Mater. Sci. **6**, 15 (1996).
[119]P. E. Blöchl, Phys. Rev. B **50**, 17953 (1994).
[120]G. Kresse and D. Joubert, Phys. Rev. B **59**, 1758 (1999).
[121]J. Heyd, J. E. Peralta, G. E. Scuseria, and R. L. Martin, J. Chem. Phys. **123**, 174101 (2005).
[122]I. C. Gerber, J. G. Ángyán, M. Marsman, and G. Kresse, J. Chem. Phys. **127**, 054101 (2007).
[123]M. Marsman, J. Paier, A. Stroppa, and G. Kresse, J. Phys.: Condens. Matter **20**, 064201 (2008).
[124]C. Franchini, R. Podloucky, J. Paier, M. Marsman, and G. Kresse, Phys. Rev. B **75**, 195128 (2007).
[125]C. Franchini, T. Archer, J. He, X.-Q. Chen, A. Filippetti, and S. Sanvito, Phys. Rev. B **83**, 220402 (2011).
[126]A. Stroppa and S. Picozzi, Phys. Chem. Chem. Phys. **12**, 5405 (2010).
[127]A. Stroppa and G. Kresse, New J. Phys. **10**, 063020 (2004).
[128]C. Franchini, J. Zabloudil, R. Podloucky, F. Allegretti, F. Li, S. Surnev, and F. P. Netzer, J. Chem. Phys. **130**, 124707 (2009).
[129]J. B. Varley, A. Janotti, C. Franchini, and C. G. Van de Walle, Phys. Rev. B **85**, 081109(R) (2012).
[130]I. de P. R. Moreira, F. Illas, and R. L. Martin, Phys. Rev. B **65**, 155102 (2002), and references therein.
[131]X. Feng and N. M. Harrison, Phys. Rev. B **70**, 092402 (2004).
[132]A. V. Krukau, O. A. Vydrov, A. F. Izmaylov, and G. Scuseria, J. Chem. Phys. **125**, 224106 (2006).
[133]F. Gygi and A. Baldereschi, Phys. Rev. Lett. **62**, 2160 (1989).
[134]S. J. Clark and J. Robertson, Phys. Rev. B **82**, 085208 (2010).
[135]A. Alkauskas, P. Broqvist, and A. Pasquarello, Phys. Status Solidi B **248**, 775 (2010).
[136]C. Gutle, A. Savin, J. B. Krieger, and J. Chen, Int. J. Quantum Chem. **75**, 885 (1999).
[137]F. Tran and P. Blaha, Phys. Rev. Lett. **102**, 226401 (2009).
[138]R. W. Nunes and X. Gonze, Phys. Rev. B **63**, 155107 (2001).
[139]M. J. Han, T. Ozaki, and J. Yu, Phys. Rev. B **73**, 045110 (2006).
[140]I. V. Solovyev and P. H. Dederichs, Phys. Rev. B **49**, 6736 (1994).
[141]A. Chainani, M. Mathew, and D. D. Sarma, Phys. Rev. B **46**, 9976 (1992).
[142]T. Mizokawa and A. Fujimori, Phys. Rev. **51**, 12880 (1995).
[143]D. D. Sarma and A. Chainani, J. Solid State Chem. **111**, 208 (1994).
[144]T. Saitoh, A. E. Bocquet, T. Mizokawa, H. Namatame, A. Fujimori, M. Abbate, Y. Takeda, and M. Takano, Phys. Rev. B **51**, 13942 (1995).
[145]M. Abbate, J. C. Fuggle, A. Fujimori, L. H. Tjeng, C. T. Chen, R. Potze, G. A. Sawatzky, H. Eisaki, and S. Uchida, Phys. Rev. B **47**, 16124 (1993).
[146]C. Franchini, V. Bayer, R. Podloucky, J. Paier, and G. Kresse, Phys. Rev. B **72**, 045132 (2005).
[147]S. Geller, Acta Crystallogr. **10**, 243 (1957).
[148]M. Cwik, T. Lorenz, J. Baier, R. Müller, G. André, F. Bourée, F. Lichtenberg, A. Freimuth, R. Schmitz, E. Müller-Hartmann, and M. Braden, Phys. Rev. B **68**, 060401 (2003).
[149]D. A. Maclean, H. N. Ng, and J. E. Greedan, J. Solid State Chem. **30**, 35 (1979).
[150]P. Bordet, C. Chaillout, M. Marezio, Q. Huang, A. Santoro, S-W. Cheong, H. Takagi, C. S. Oglesby, and B. Batlogg, J. Solid State Chem. **106**, 253 (1993).
[151]C. P. Khattak and D. E. Cox, Mater. Res. Bull. **12**, 463 (1977).
[152]K. Tezuka, Y. Hinatsu, A. Nakamura, T. Inami, Y. Shimojo, and Y. Morii, J. Solid State Chem. **141**, 404 (1998).
[153]G. Li, X. Kuang, S. Tian, F. Liao, X. Jing, Y. Uesu, and K. Kohn, J. Solid State Chem. **165**, 381 (2002).
[154]J. B. A. A. Elemans, B. van Laar, K. R. van der Veen, and B. O. Loopstra, J. Solid State Chem. **3**, 238 (1971).
[155]S. E. Dann, D. B. Currie, M. T. Weller, M. F. Thomas, and A. D. Al-Rawwas, J. Solid State Chem. **109**, 134 (1994).
[156]P. G. Radaelli and S. W. Cheong, Phys. Rev. B **66**, 094408 (2002).
[157]G. Thornton, B. C. Tofield, and A. W. Hewat, J. Solid State Chem. **61**, 301 (1986).
[158]O. Haas, R. P. W. J. Struis, and J. M. McBreen, J. Solid State Chem. **177**, 1000 (2004).
[159]J. L. García-Muñoz, J. Rodríguez-Carvajal, P. Lacorre, and J. B. Torrance, Phys. Rev. B **46**, 4414 (1992).
[160]S. Darracq, S. Matar, and G. Demzeau, Solid State Commun. **85**, 961 (1993).
[161]J. F. Bringley, B. A. Scott, S. J. La Placa, T. R. McGuire, F. Mehran, M. W. McElfresh, and D. E. Cox, Phys. Rev. B **47**, 15269 (1993).
[162]I. de P. R. Moreira and F. Illas, Phys. Chem. Chem. Phys. **8**, 1645 (2006).
[163]V. V. Afans'ev, A. Stesmans, C. Zhao, M. Caymax, T. Heeg, J. Schubert, Y. Jia, D. G. Schlom, and G. Lucovsky, Appl. Phys. Lett. **85**, 5917 (2004).
[164]J. Hemberger, H.-A. Krug von Nidda, V. Fritsch, J. Deisenhofer, S. Lobina, T. Rudolf, P. Lunkenheimer, F. Lichtenberg, A. Loidl, D. Bruns, and B. Büchner, Phys. Rev. Lett. **91**, 066403 (2003).
[165]B. Keimer, D. Casa, A. Ivanov, J. W. Lynn, M. V. Zimmermann, J. P. Hill, D. Gibbs, Y. Taguchi, and Y. Tokura, Phys. Rev. Lett. **85**, 3946 (2000).
[166]Y. Okimoto, T. Katsufuji, Y. Okada, T. Arima, and Y. Tokura, Phys. Rev. B **51**, 9581 (1995).
[167]S. V. Streltsov, A. S. Mylnikova, A. O. Shorikov, Z. V. Pchelkina, D. I. Khomskii, and V. I. Anisimov, Phys. Rev. B **71**, 245114 (2005).
[168]H. Fujitani and S. Asano, Phys. Rev. B **51**, 2098 (1995).
[169]H. Sawada and K. Terakura, Phys. Rev. B **58**, 6831 (1998).
[170]E. Pavarini, S. Biermann, A. Poteryaev, A. I. Lichtenstein, A. Georges, and O. K. Andersen, Phys. Rev. Lett. **92**, 176403 (2004).
[171]I. V. Solovyev, Phys. Rev. B **69**, 134403 (2004).
[172]J. P. Goral and J. E. Greedan, J. Magn. Magn. Mater. **37**, 315 (1983).
[173]D. Gryaznov, E. Heifetsa, and E. Kotomin, Phys. Chem. Chem. Phys. **14**, 4482 (2012).
[174]H. Roth, Ph.D. thesis, Universität zu Köln, Germany, 2008, http://kups.ub.uni-koeln.de/2335/.
[175]V. G. Zubkov, G. V. Bazuev, V. A. Perelyae, and G. P. Shveikin, Fizika Tverdogo Tela **15**, 1610 (1973) [Sov. Phys. Solid State **15**, 1078 (1973)].
[176]W. C. Koehler and E. O. Wollan, J. Phys. Chem. Solids **2**, 100 (1957).
[177]E. F. Bertaut, J. Mareschal, G. De Vries, R. Aleonard, R. Pauthenet, J. P. Rebouillat, and V. Zarubicka, IEEE Trans. Magn. **2**, 453 (1966).
[178]N. Sakai, H. Fjellvaĝ, and B. C. Hauback, J. Solid State Chem. **121**, 202 (1996).

[179] W.-G. Yin, D. Volja, and W. Ku, Phys. Rev. Lett. **96**, 116405 (2006).
[180] E. Pavarini and E. Koch, Phys. Rev. Lett. **104**, 086402 (2010).
[181] J. H. Jung, K. H. Kim, D. J. Eom, T. W. Noh, E. J. Choi, J. Yu, Y. S. Kwon, and Y. Chung, Phys. Rev. B **55**, 15489 (1997).
[182] J. H. Jung, K. H. Kim, T. W. Noh, E. J. Choi, and J. Yu, Phys. Rev. B **57**, R11043 (1998).
[183] R. Krüger, B. Schulz, S. Naler, R. Rauer, D. Budelmann, J. Bäckström, K. H. Kim, S-W. Cheong, V. Perebeinos, M. Rübhausen, Phys. Rev. Lett. **92**, 097203 (2004).
[184] F. Moussa, M. Hennion, J. Rodríguez-Carvajal, H. Moudden, L. Pinsard, and A. Revcolevschi, Phys. Rev. B **54**, 15149 (1996).
[185] B. C. Hauback, H. Fjellvåg, and N. Sakai, J. Solid State Chem. **124**, 43 (1996).
[186] J. Rodríguez-Carvajal, M. Hennion, F. Moussa, A. H. Moudden, L. Pinsard, and A. Revcolevschi, Phys. Rev. B **57**, R3189 (1998).
[187] R. L. White, J. Appl. Phys. **40**, 1061 (1969).
[188] M. B. Bellakki, B. J. Kelly, and V. Manivannan, J. Alloys Compd. **489**, 64 (2010).
[189] X. D. Zhou, L. R. Pederson, Q. Cai, J. Yang, B. J. Scarfino, M. Kim, W. B. Yelon, W. J. James, H. U. Anderson, and C. Wang, J. Appl. Phys. **99**, 08M918 (2006).
[190] H. Wadati, D. Kobayashi, H. Kumigashira, K. Okazaki, T. Mizokawa, A. Fujimori, K. Horiba, M. Oshima, N. Hamada, M. Lippmaa, M. Kawasaki, and H. Koinuma, Phys. Rev. B **71**, 035108 (2005).
[191] J. B. Goodenough, *Localized to Itinerant Electronic Transition in Perovskite Oxides* (Springer, New York, 2001), and references therein.
[192] C. N. R. Rao, Md. Motin Seikh, and C. Narayana, Top. Curr. Chem. **234**, 1 (2004), and references therein.
[193] S. Yamaguchi, Y. Okimoto, H. Taniguchi, and Y. Tokura, Phys. Rev. B **53**, R2926 (1996).
[194] K. Sreedhar, J. M. Honig, M. Darwin, M. McElfresh, P. M. Shand, J. Xu, B. C. Crooker, and J. Spalek, Phys. Rev. B **46**, 6382 (1992).
[195] D. D. Sarma, N. Shanthi, and P. Mahadevan, J. Phys.: Condens. Matter **6**, 10467 (1994).
[196] V. I. Anisimov, D. Bukhvalov, and T. M. Rice, Phys. Rev. B **59**, 7901 (1999).
[197] M. K. Stewart, C.-H. Yee, Jian Liu, M. Kareev, R. K. Smith, B. C. Chapler, M. Varela, P. J. Ryan, K. Haule, J. Chakhalian, and D. N. Basov, Phys. Rev. B **83**, 075125 (2011).
[198] P. Hansmann, A. Toschi, X. Yang, O. K. Andersen, and K. Held, Phys. Rev. B **82**, 235123 (2010).
[199] X. Deng, M. Ferrero, J. Mravlje, M. Aichhorn, and A. Georges, Phys. Rev. B **85**, 125137 (2012).
[200] T. Mizokawa, A. Fujimori, H. Namatame, Y. Takeda, and M. Takano, Phys. Rev. **57**, 9550 (1998).
[201] K. Okada and A. Kotani, J. Phys. Soc. Jpn. **68**, 666 (1999).
[202] G. Yalovega and A. V. Soldatov, Phys. Status Solidi B **218**, 455 (2000).
[203] T. Arima and Y. Tokura, J. Phys. Soc. Jpn. **64**, 2488 (1995).
[204] M. Mochizuki and M. Imada, Phys. Rev. Lett. **91**, 167203 (2003).
[205] T. Kiyama and M. Itoh, Phys. Rev. Lett. **91**, 167202 (2003).
[206] J. B. Goodenough, Prog. Solid State Chem. **5**, 145 (1971).
[207] Y. Ren, A. A. Nugroho, A. A. Menovsky, J. Strempfer, U. Rütt, F. Iga, T. Takabatake, and C. W. Kimball, Phys. Rev. B **67**, 014107 (2003).
[208] Y. Murakami, J. P. Hill, D. Gibbs, M. Blume, I. Koyama, M. Tanaka, H. Kawata, T. Arima, Y. Tokura, K. Hirota, and Y. Endoh, Phys. Rev. Lett. **81**, 582 (1998).
[209] N. N. Kovaleva, A. V. Boris, C. Bernhard, A. Kulakov, A. Pimenov, A. M. Balbashov, G. Khaliullin, and B. Keimer, Phys. Rev. Lett. **93**, 147204 (2004).
[210] M. Nakamura, T. Yoshida, K. Mamiya, A. Fujimori, Y. Taguchi, and Y. Tokura, Mater. Sci. Eng. B **68**, 123 (1999).
[211] K. Maiti and D. D. Sarma, Phys. Rev. B **61**, 2525 (2000).
[212] D. D. Sarma, N. Shanthi, and P. Mahadevan, Phys. Rev. B **54**, 1622 (1996).
[213] M. Abbate, G. Zampieri, F. Prado, A. Caneiro, J. M. Gonzalez-Calbet, and M. Vallet-Regi, Phys. Rev. B **65**, 155101 (2002).